MODELLING, FABRICATION AND MICROSTRUCTURAL ANALYSIS OF SELECTIVELY LASER MELTED Ti64 POROUS SCAFFOLDS FOR BIOMEDICAL APPLICATION

A thesis submitted towards partial fulfillment of the requirements for the degree of

Master of Technology in Laser Technology

Submitted by

ADIL WAZEER

Examination Roll No: M4LST22002

Registration No: 154557 of 2020-21

Under the guidance of

Dr. Amit Karmakar

Professor and HOD

Mechanical Engineering Department

Jadavpur University, Kolkata

Dr. Apurba Das

Assistant Professor

Dept. of Aerospace Engg. and Applied Mechanics

IIEST, Shibpur

School of Laser Science and Engineering

Faculty of Interdisciplinary Studies, Law and Management

Jadavpur University

Kolkata-700032

India

2022

M.Tech in Laser Science and Technology
Course affiliated to
Faculty of Engineering and Technology
and offered by
Faculty of Interdisciplinary Studies, Law and Management
Jadavpur University
Kolkata, India

CERTIFICATE OF RECOMMENDATION

THIS IS CERTIFIED THAT THE THESIS ENTITLED "**MODELLING, FABRICATION AND MICROSTRUCTURAL ANALYSIS OF SELECTIVELY LASER MELTED Ti64 POROUS SCAFFOLDS FOR BIOMEDICAL APPLICATION**" IS A BONAFIDE WORK CARRIED OUT BY **ADIL WAZEER** UNDER MY SUPERVISION AND GUIDANCE FOR PARTIAL FULFILLMENT OF THE REQUIREMENT FOR POST GRADUATE DEGREE OF MASTER OF TECHNOLOGY IN LASER TECHNOLOGY DURING THE ACADEMIC SESSION 2021-2022.

……

Thesis Supervisors

Dr. Amit Karmakar
Professor
Department of Mechanical Engineering
Jadavpur University
Kolkata-700032

&

Dr. Apurba Das
Assistant Professor
Dept. of Aerospace Engg. and
Applied Mechanics
IIEST, Shibpur-711103

……

Sri. Dipten Misra
Director, School of Laser Science and Engineering
Jadavpur University, Kolkata-700032

……...

Dean
Faculty of Interdisciplinary Studies, Law and Management
Jadavpur University, Kolkata-700032

M.Tech in Laser Science and Technology
Course affiliated to
Faculty of Engineering and Technology
and offered by
Faculty of Interdisciplinary Studies, Law and Management
Jadavpur University
Kolkata, India

CERTIFICATE OF APPROVAL**

This foregoing thesis is hereby approved as a creditable study of an engineering subject carried out and presented in a manner satisfactory to warrant its acceptance as a pre-requisite to the degree for which it has been submitted. It is understood that by this approval the undersigned do not necessarily endorse or approve any statement made, opinion expressed or conclusion drawn therein but approve the thesis only for the purpose for which it has been submitted.

Committee of final examination for evaluation of thesis

……
……
……

**Only in case the recommendation is concurred

DECLARATION OF ORIGINALITY AND COMPLIANCE OF ACADEMIC ETHICS

The author hereby declares that this thesis contains original research work by the undersigned candidate as part of his Master of Technology in Laser Technology studies during academic session 2021-2022.

All information in this document has been obtained and presented in accordance with academic rules and ethical conduct.

The author also declares that as required by the rules and conduct, the author has fully cited and referred all material and results that are not original to this work.

NAME: **ADIL WAZEER**

EXAMINATION ROLL NO.:**M4LST22002**

THESIS TITLE: **MODELLING, FABRICATION AND MICROSTRUCTURAL ANALYSIS OF SELECTIVELY LASER MELTED Ti64 POROUS SCAFFOLDS FOR BIOMEDICAL APPLICATION**

SIGNATURE: DATE:

ACKNOWLEDGEMENT

First and foremost, I thank almighty Allah (God) for giving me the ability and patience and blessing me with success to complete this thesis.

I would like to gratefully thank my academic supervisors, Prof. Amit Karmakar and Dr. Apurba Das; it is truly a pleasure working under them, for their unlimited support, continuous encouragement and durable patience during my project. Because of their close supervision and great knowledge and professionalism I have experienced a significant event in my life with a positive effect to a promising future.

I would also like to express my deep sense of thankfulness to Sri. Dipten Misra for providing me the proper atmosphere of work.

I would also want to express my gratitude to my lab seniors and research scholars, Subhrajyoti Sarkar and Palash Mondal for making this journey a happy and a joyous one.

Finally, special thanks to my parents and sister whom always they supportme and worry about me no matter how old I am, encouraging me while I am far away from them &fortheir patience, time and understanding.

ADIL WAZEER
Examination Roll No: M4LST22002
Registration No: 154557 of 2021-21

List of figures

Figure 1: A) HCP Structure B) BCC Structure

Figure 2: SEM micrograph of Porous Ti

Figure 3: Elastic moduli of different biomedical alloys and bone

Figure 4: a) SEM micrographs illustrating the surface characteristics of rhombic dodecahedron structural Ti–24Nb–4Zr–8Sn scaffolds generated by EBM and SLM, and b) melting schematic diagram

Figure 5: Characteristic porous CP–Ti microstructures having a porosity of 55% and varying pore sizes: a) 125mm, b) 250mm, c) 400mm, and d) 800mm

Figure 6: Schematic of selective laser melting (SLM) parameters

Figure 7: Different SLM processing patterns: (a) Uni-directional scanning, (b) Bi-directional scanning (zigzag) scanning, (c) Inter-layer scanning, and (d) Interlayer rotation scanning

Figure 8: Optical microstructures of the SLM-produced Ti–24Nb–4Zr-8Sn part, showing porosity and un-melted areas due to improper SLM processing parameters

Figure 9: Scanning electron microscopy (SEM) image showing balling effect in SLM-processed CP–Ti

Figure 10: Human Bone Structure

Figure 11: SEM of a 22-Year Old Male Human Bone

Figure 12: Image of Ti-6Al-4V powder of spherical shape

Figure 13: Particle size distribution of Ti-6Al-4V powder

Figure 14: An overview of additive manufacturing process employed

Figure 15: Computer layout of models on the machine bed

Figure 16: Actual picture of the manufactured samples on machine bed

Figure 17: EOS direct metal laser sintering machine (model: EOSINT-M280) installed at Central Tool Room and Training Center, Bhubaneswar, Odisha

Figure 18. Schematic of typical Selective Laser Melting (SLM) process for fabrication of Ti64 porous lattice structures using SLM system EOSINT-M280

Figure 19. SLM manufacturing process

Figure 20: Fabricated Ti-6Al-4V porous scaffolds by SLM technique: (a) Diamond, (b) Cross, (c) Grid, (d) Vinties

Figure 21: Porosity measurement by measuring cylinder: (a) cross, (b) diamond, (c) vinties, (d) grid

Figure 22: Porosity percentage error of scaffolds

Figure 23. Effect of input process parameters of Ti-6Al-4V scaffolds during SLM

Figure 24. Talysurf surface roughness tester (Mitutoyo SJ-210)

Figure 25: Upper HSS plate to be fitted in top part on INSTRON machine, b lower HSS plate where samples will be kept and to be fitted at the bottom part on INSTRON machine

Figure 26: Sample held in INSTRON testing machine with two additional attachments

Figure 27: Experimental setup for compression test on INSTRON

Figure 28: Stress–strain curve for compression test of scaffolds

Figure 29: Relative elastic modulus, E_1/E_2vs porosity %.

Figure 30: Relative compressive strength, σ_1/σ_2vs porosity %

Figure 31: Main Effects Plots for Means and SN Ratios for Diamond

Figure 32: Main Effects Plots for Means and SN Ratios for Cross

Figure 33: Main Effects Plots for Means and SN Ratios for Grid

Figure 34: Main Effects Plots for Means and SN Ratios for Vinties

Figure 35: The Stereo Microscope (ZEISS Stemi 508)

Figure 36: Microscopic image of diamond scaffold

Figure 37: Microscopic image of diamond scaffold with observed markings

Figure 38: Microscopic image of cross scaffold

Figure 39: Microscopic image of cross scaffold with observed markings

Figure 40: Microscopic image of grid scaffold

Figure 41: Microscopic image of grid scaffold with observed markings

Figure 42: Microscopic image of vinties scaffold

Figure 43: Microscopic image of vinties scaffold with observed markings

List of tables

Table 1: Outline of additive manufacturing approaches

Table 2: Scaffolding Requirements for Implants

Table 3: Typical Metallic Implant Materials' Properties

Table 4: Chemical composition of Ti-6Al-4V powder

Table 5: Particle size distribution analysis

Table 6: Powder property analysis

Table 7: Input process parameters used in SLM process for Ti-6Al-4V.

Table 8: Heat treatment process of as-built scaffolds by SLM

Table 9: Measured porosity of the fabricated scaffolds

Table 10: Surface roughness value (Ra) of prepared samples measured using Talysurf surface roughness tester

Table 11: Response Table for Signal to Noise Ratio (Diamond)

Table 12: Response Table for Means (Diamond)

Table 13: Response Table for Signal to Noise Ratios (Cross)

Table 14: Response Table for Means (Cross)

Table 15: Response Table for Signal to Noise Ratios (Grid)

Table 16: Response Table for Means (Grid)

Table 17: Response Table for Signal to Noise Ratio (Vinties)

Table 18: Response Table for Means (Vinties)

Table 19: General specifications of the microscope

Table of Contents

Certificate of Recommendation *i*
Certificate of Approval *ii*
Declaration of Originality *iii*
Acknowledgement *iv*
List of Figures *v*
List of Tables *vii*

1. Introduction **1**
1.1 Background 1
1.2 Ti-6Al-4V 2
1.3 Additive Manufacturing (AM) 3
1.4 Selective Laser Melting (SLM) 6
1.5 Objectives of the study 7
1.6 Organization of the thesis 7
2. Literature Survey **8**
2.1 Titanium 8
2.1.1 Titanium as a biomaterial 9
2.1.2 Porous Scaffolds 10
2.1.3 Biomedical Titanium Alloys 11
2.2 New preparation methods for Ti alloys for biomedical application 12
2.2.1 Selective Laser Melting 12
2.2.2 Electron Beam Melting 14
2.2.3 Preparation methods of porous scaffolds 15
2.3 Selective Laser Melting (SLM) Process and Processing parameters involved 18
2.3.1 Process Parameters Involved 19

2.3.2 Needs of developing new alloy powder materials for SLM 21
2.3.3 Defects and Unfavorable Issues in SLM 22
2.3.4 SLM produced Ti based materials 24
2.4 Human Bone 25
3. Material and Methodology 27
3.1 Powder Material 27
3.2 Modelling of Ti-6Al-4V scaffolds 29
3.3 Fabrication of Ti64 scaffolds employing Selective Laser Melting 31
3.4 Heat Treatment Process 35
4. Study of Mechanical Characteristics 36
4.1 Porosity 36
4.2 Surface Roughness Test 39
4.3 Compression Test 40
5. Optimization of porosity results 45
6. Microscopic study of scaffolds 52
7. Conclusions 58
Future Scope of Work 60
References 61

Chapter 1

Introduction

1.1 Background

For years, metallic materials are being utilised and researched for biomedical applications. They comprise bionic implants, dental work, and orthopaedic prosthesis implants, which substitute defective or damaged human body parts and tissues. Each year, millions of patients profit with biomedical implants that successfully restore functionality or replace decaying portions [1]. Metallic materials and applied materials namely stainless steel (SS), Cr-based alloys, niobium, tantalum, Ti, and titanium alloys were employed in biomedical uses throughout the last several decades [2]. Furthermore, mechanical qualities of a wide range of biomedical materials have been improved, including corrosion resistance, bio-adhesion, and biocompatibility [3]. Metallic bone implants, on the other hand, have a greater density than natural bones. This has detrimental repercussions since it is challenging for natural bone to regenerate within solid or thick artificial portions. Furthermore, the rigidity of metallic implants is significantly greater than that of bone tissue, resulting in 'stress shielding' at the bone tissue/implant interface, that results in cell migration and bone deterioration in the long term. As a conclusion, there is a rising desire for implants which could give a suitable resolution to the concerns highlighted by standard medical implants.

The goal of scientific study is to produce porous materials to complement solid implants. Porous metallic materials with tailored physical characteristics and biocompatibility were designed for orthopaedic applications [4, 5]. Spinal fixation devices, fixation screws, and bone scaffolds are examples of orthopaedic uses [6]. Metallic scaffolds were enhanced having a structure comparable to natural bone structure and comparable mechanical property values (lower Young's modulus which mimics natural bone elasticity by obtaining appropriate stress characteristics).

Nonmetallic porous materials, on the other hand (particularly porous ceramics and polymers), are still not robust enough to bear ordinary physiological stresses and thus are regarded to have poor mechanical qualities. As a result, implants made of this substance are often utilised mainly for soft tissue growth and cushioning bone deterioration. Hard tissues, like hip joint implants, demand substantially greater mechanical characteristics, making metals & alloys ideal for this use [8]. Ti and its alloys, particularly, were regarded as being frequently selected material because to its biocompatibility, resistance to corrosion, and strength-to-weight ratio [8]. Due to the general discrepancy among bone (10-30 GPa) and metallic implants, metallic material elasticity is a key problem in medical implants (110 GPa for Ti). Young's modulus of hard tissue is typically 10-20 times lower than most metals, hence considerable study is focused on lowering its number by improving porosity in the material or reducing Young's modulus of elasticity by developing low-stiffness alloys.

1.2 Ti-6Al-4V

Because of its biocompatibility, the majority of Ti6Al4V research is motivated by its prospective uses as body prosthesis and implants. Ti6Al4V is of particular relevance due to its uses in the biomedical industry [9]. Because of its superb biocompatibility, exceptional corrosion resilience, and superior mechanical durability, Ti6Al4V has indeed been extensively employed for different orthopaedic implants [10]. Furthermore, Ti6Al4V has a higher specific strength and elastic modulus over cobalt chromium alloys and stainless steel [11]. ASTM standards, ISO standards, and the US FDA all specify functional standards for Ti6Al4V implants. Regardless of how the alloy is processed, Ti6Al4V components could have a variety of microstructures.Casting, wrought ingots, and powder metallurgy, for instance, provide three distinct microstructures for Ti6Al4V. It is due to the microstructure of pure titanium is entirely α. B Phase occurs along grain boundary whenever pure titanium is alloyed with stabilisers. The proportion of α and β changes based on the treatment parameters like temperature, cooling rates, and mechanical functioning degree.

The price of titanium alloys originates primarily from 2 factors: I the expenses associated to its extraction technique (the presently utilised Kroll’s reduction procedure is energy-intensive and not so far robust) and (ii) the pay of the current manufacturing processing which needs

preventive habitats, greater energy intake and usually entails substantial waste production [12]. To reduce the aggregate expense of manufacturing, study has thus centred on unconventional effectual manufacturing methods [13]. In recent times, additive manufacturing (AM) has sparked considerable interest in addressing a few of these difficulties. In theory, additive manufacturing permits one to create an object of practically any desirable shape via a digital model using sequential layers of material placed and fused together.

Aside from the ability to build components with unique functional geometries those are hard to obtain with traditional processing, the usage of AM is connected with a slew of other benefits [14]. For instance, excluding support structures in certain circumstances, AM employs only the raw material required to build a component, regardless of its form, minimizing material waste dramatically. Selective Laser Melting is among the most intriguing AM methods for the manufacturing of titanium alloys (SLM). Following precise adjustment of the SLM system, literatures have revealed that exceptionally dense (99.7 percent or higher) SLM titanium alloy may be created.As a result, super dense SLM titanium alloys have mechanical qualities equivalent to those of traditionally made alloys. The preponderance of titanium alloy SLM research has, though, concentrated on selecting processing parameters which could enhance sample density and construct rate with minimal respect for component microstructure. As a result, whenever multiple SLM systems are employed, component grade, consistency, and mechanical characteristics of SLM specimens are frequently uneven.

1.3 Additive Manufacturing (AM)

In contrast to conventional subtractive or deformation-based fabrication processes, additive manufacturing (AM) pertains to a series of production processes in which things are built from three-dimensional (3D) model data by connecting materials, generally layer upon layer [15]. AM approaches evolved from Rapid Prototyping (RP) methods that were established in the late 1980s and early 1990s in response to a demand for the creation of complicated shaped prototypes in extremely short lead times. Following several advances in the 2000s, a few of the RP processes have grown into dependable production procedures proficient of treating wide array of materials. Due to prevalence of concurrent advances, additive manufacturing methods are also known as free-form fabrication, direct digital manufacturing, fast manufacturing, (additive) layer

manufacturing, additive fabrication, additive techniques, 3D printing or additive processes [15, 16].

All AM methods use the identical manufacturing process. To begin, a 3D model of the part must be created and converted to the Standard Triangulation Language (STL) format. There are various techniques to generate model data. Most apparent method is to utilize 3D computer assisted design (CAD) software to create the part. The drawing could also be derived from a point cloud geometry measurement or from computed tomography data. The 3D model is further divided into thin layers, or 'slices.' Based on the AM process, a collection of scanning or deposition path vectors is created for these product slices. Finally, the digital data is transferred to the AM machine, which constructs the product layer - by - layer. The most frequent AM approaches are 3D-printing (3D-P), stereolithography (SLA), Electron Beam Melting (EBM), Selective Laser Melting (SLM), Laser Engineered Net Shaping (LENS) and Laser Cladding (LC).

Both SEM and EBM are full-melt powder bed fusion AM processes wherein heat is provided via laser beam along with electron beam, correspondingly. To reduce electromagnetic charge of the metal powder in EBM, mainly nonmagnetic metals may be utilised, and the powder particles were sintered selectively first before melting. This difficulty is eliminated by the usage of a laser beam in SLM, and in principle, any metal with a high absorptivity for the specified laser light may be employed. The pre-heating necessary for sintering in EBM results in a chamber temperature of up to 700 °C [17]. Presently, the SLM technique is carried out at temperatures varying from ambient temperature to 200 °C. In contrast to SLM components, the greater ambient temperature in EBM leads in reduced thermal gradients, lowering thermal stresses and the existence of meta-stable phases [18]. Additionally, unlike EBM, the atmosphere in SLM is often economically clean Ar or N_2 gas, resulting in reduced oxidation or contamination of the melt pool. Furthermore, the reduced ambient pressure throughout EBM encourages preferred evaporation of alloying elements, resulting in a shift in chemical composition [19]. Aside from having a larger material palette, the SLM method also has a greater resolution and improved surface roughness than EBM procedure [17]. The table 1 below provides an overview of several AM methods.

Table 1: Outline of additive manufacturing approaches.

	Process	layout	layer creation method	Phase change	Materials
LIQUID	**Stereolithography (SLA)**	Liquid resin in a vat	Liquid layer deposition	Photo-polymerisation	Acrylates, epoxies, filled resins
	Fused deposition modelling (FDM)	Material melted in a nozzle	Continuous extrusion and deposition	Solidification by cooling	Polymer (ABS, PA), wax, filled polymers, metals
	Ink jet printing	Droplets of molten material	Drop on demand deposition	Solidification by cooling	Polymers, wax
POWDER	**Three-dimensional printing**	Binder and powder in bed	Layer of powder and drop on demand deposition	No phase change	Ceramics/metals/polymers with binder
	Selective laser sintering/melting (SLS/SLM)	Powder in bed	Layer of powder	Sintering/melting by laser and resolidification by cooling	(Filled) polymers, metals with binder, (pure) metals, ceramics (with binder)
	Electron Beam Melting (EBM)	Powder in bed	Layer of powder	Melting by electron beam and resolidification by cooling	Non-magnetic metals
	Laser Cladding (LC)	Powder delivery through nozzle	Continuous injection of powder	Laser melting and solidification by cooling	Metals
SOLID	**Laminated object manufacturing (LOM) and variants**	Feeding, cutting and binding of sheets	Deposition of sheet material	No phase change	Paper, polymer (foam), composites, metals, ceramics
	Shape Metal Deposition (SMD)	Metal wire delivery through nozzle	Continuous injection of powder	Laser melting and solidification by cooling	Metals
VAPOUR	**Selective Laser Chemical Vapour Deposition**	Gas flow in laser	Condensation of gas	Forming solid material from gas by chemical decomposition	Metals, ceramics

1.4 Selective Laser Melting (SLM)

Selective Laser Melting (SLM) is an AM method which emerged in the 1980s and early 1990s [20]. A product is created using the SLM technique by selectively melting consecutive layers of powder employing the action of beam of laser. The powder material is heated by radiation, and if enough energy is provided, the substance melts and produces a liquid pool. The molten pool swiftly solidifies and cools following interacting with laser beam and the compacted material become part of the finished product. Following scanning the cross sections of all layers within this batch, the build base is lowered by the coating thickness and application of fresh powder layer is done. Cycle is continued till product is finished. Non-irradiated material stays in the build cylinder and serves as scaffolding for the layers that followed. The leftover powder is filtrated and recycled after the procedure. The pieces are created connected to a solid substrate to prevent curling of the solidified material caused by the buildup of thermal stresses during SLM process. To prevent contaminating of the melt pool or oxidation of solidified material, the operation is carried out in an inert environment.

Selective Laser Melting, also known as Laser Melting (LM), Laser Beam Melting (LBM), Direct Metal Laser Re-melting (DMLR) or Direct Metal Laser Sintering (DMLS) is a methodology that utilizes higher power density laser beam for melting sequential layers of metallic powders to build 3D objects. Such goods are utilised not just for prototyping, but as structural components.

The key strengths of Selective Laser Melting technology are the product geometric flexibility and the method adaptability. On one side, the process's versatility is seen in the simplicity of modifying the product form shortly prior manufacturing that greatly reduces lead time and time-to-market. SLM, on either hand, demonstrates a significant degree of versatility in terms of the number of different-shaped items that may be built in a single batch. Products with intricate internal channels or lightweight porous structures could be created by introducing the material layer by layer. Moreover, diverse assembly pieces could be made as a monolithic product. The SLM method is a near-net-shape manufacturing approach that leads in much more effective raw material utilization.

1.5 Objectives of the study

a) Modeling of the four Ti64 porous scaffolds of different geometries (Diamond, Cross, Grid and Vinties) for further implementation regarding the purpose of fabrication.
b) Fabrication of the Ti64 scaffolds implementing the method of Selective Laser Melting.
c) Mechanical tests of the fabricated scaffolds.
d) Porosity Parameter Optimization study using Optimization tool Minitab.
e) Microstructural study of the four Ti64 scaffolds (Diamond, Cross, Grid and Vinties).

1.6 Organization of the thesis

This thesis starts with the introduction section, elaborating the background of research and stating the objectives of the present study in Chapter 1.

It is then followed by literature survey to present associated theory, methods and findings of past research in Chapter 2.

Chapter 3 gives details of the material and methodology implemented in the manufacturing of the scaffolds (powder material, modeling of scaffolds and fabrication using SLM technique).

The study of mechanical characteristics such as surface roughness, porosity and compression test of the scaffold is presented in chapter 4.

Chapter 5 deals with the optimization study of the porosity parameter with respect to other processing parameters. Microscopic study of the Ti64 scaffolds is presented in chapter 6. Finally, concluding with future scope of the present work and conclusions.

Chapter 2

Literature Survey

2.1 Titanium

Ti possesses a hexagonal closed-packed (HCP) structure at room temperature, which generally is termed as α [21]. Ti undergoes an allotropic change to body-centered cubic (BCC) β structure at 882.5°C and remains stable in the β-phase till it achieves its melting point of 1678°C [21, 22]. Figure 1 depicts the body cell for these structures. Ti alloys could have α, β or mixed α/β microstructures owing to the allotropic transition that is impacted by replacement and intervening elements and is reliant on metal purity [22].

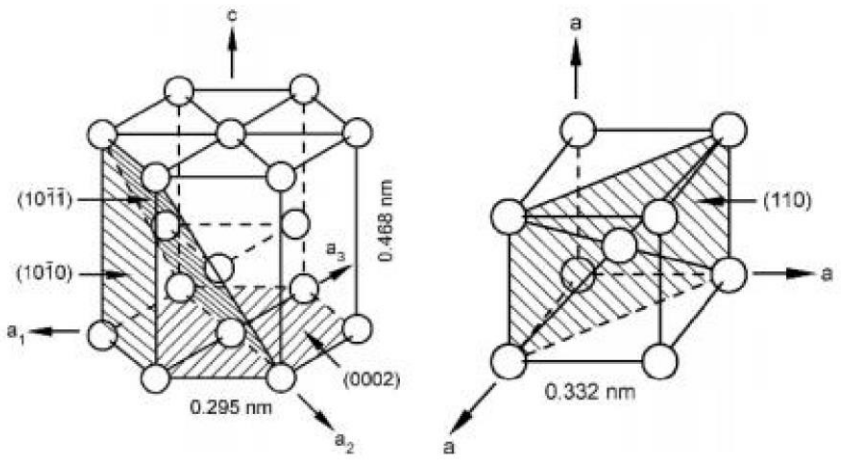

Figure 1: A) HCP Structure B) BCC Structure [22].

Ti alloys are created by alloying elements stabilizing between the α or β phases, and the amount of bonding electrons engaged is depending on the degree of bonding electrons participating. Electron/atom ratios of alloying elements lower than 4 stabilize the phase, ratios of 4 neutralize the phase, and ratios larger than 4 stabilize the β phase [23]. The β -phase has substantial anisotropy from α, physical and mechanical characteristics, lesser ductility, elevated opposition

to plastic deformation, greater creep resistance, as well as diffusion rates at least two orders of magnitude lesser than β-phase [23].

2.1.1 Titanium as a Biomaterial

Scaffolds comprised of alloys like stainless steel, cobalt, and titanium have long being employed inside the human body [24]. The table 2 lists the several standards which these biomaterials should fulfill in order to be employed in biological applications. Table 3 lists some of the features of these metals and alloys.

Table 2: Scaffolding Requirements for Implants [25].

COMPATIBILITY	MECHANICAL PROPERTIES	MANUFACTURING

• Tissue reactions
• Changes in properties
  • Mechanical
  • Physical
  • Chemical
• Degradation leads to
  • Local deleterious changes
  • Harmful systemic effects
	• Elasticity
	• Yield stress
	• Ductility
	• Toughness
	• Time dependent deformation
	• Creep
	• Ultimate strength
	• fatigue strength
	• Hardness
	• Wear resistance
		• Fabrication methods
		• Consistency and conformity to all requirements
		• Quality of raw materials
		• Superior techniques to obtain excellent surface finish or texture
		• Capability of material to get safe and efficient sterilization
		• Cost of product

Although the table 3 lists several problems connected with particular biomaterials, Ti as well as its alloys is becoming progressively highly relevant in the market owing to its elevated qualities, which make them perfect as implant materials. Because of its great resistance to corrosion, biocompatibility, and strength, Ti and its alloys can fulfil the criteria for implants higher than any material [26].

Table 3: Typical Metallic Implant Materials' Properties [25].

	Stainless steels	Cobalt-base alloys	Ti & Ti-base alloys
Designation	ASTM F-138 ('316 LDVM')	ASTM F-75 ASTM F-799 ASTM F-1537 (Cast and wrought)	ASTM F-67 (ISO 5832/II) ASTM F-136 (ISO 5832/II) ASTM F-1295 (Cast and wrought)
Principal alloying elements (wt%)	Fe(bal.) Cr(17–20) Ni(12–14) Mo(2–4)	Co(bal.) Cr(19–30) Mo(0–10) Ni(0–37)	Ti(bal.) Al(6) V(4) Nb(7)
Advantages	• cost, availability • processing	• wear resistance • corrosion resistance • fatigue strength	• biocompatibility • corrosion • minimum modulus • fatigue strength
Disadvantages	• long term behavior • high modulus	• high modulus • biocompatibility	• power wear resistance • low shear strength
Primary utilisations	Temporary devices (fracture plates, screws, hip nails) Used for THRs stems in UK (high Nitrogen)	Dentistry castings Prostheses stems Load-bearing components in TJR (wrought alloys)	Used in THRs with modular (CoCrMo or ceramic) femoral heads Long-term, permanent devices (nails, pacemakers)

According to Lutjering and Williams [22], the main drawback of Ti is its high elastic modulus of roughly 114 GPa. Mechanical strength is an important consideration when employing scaffolds for bone replacement. The scaffold must be robust enough to handle acceptable loads, and not so strong that it causes stress shielding.

The modulus discrepancy among two materials causes stress shielding. Reduced stress is passed to bone linked to implant, resulting in bone resorption and, as a result, implant loosening [27]. Bone has a modulus of 4-30 GPa, that is much lower than Ti [28-30]. It reduces the implant's lifespan, frequently leading to uncomfortable and expensive modification operations. As a result, research has been carried out to identify novel strategies for improving mechanical characteristics of Ti and titanium alloys for biomedical purposes [27].

2.1.2 Porous Scaffolds

Porous materials have recently been explored in research. Parthasarathy et al. [31] demonstrated how Ti-based biomaterials may be tailored to human bone by including a greater porous structure that is essential for cell adhesion, growth, and survival. Researchers came to the conclusion that porous structure minimizes the elastic modulus and consequences of stiffness misalignment, which are frequent in mass metallic biomaterials. This really is due to the fact that there is far lower material sustaining same cross-sectional area.

Furthermore, porosity produces an open channel which favors tissue ingrowth and hence allows for improved tissue conduction [27]. The linked structure enables for full bone ingrowth and a steady blood supply, both of which are critical for biocompatibility and been a source of concern in previous biomaterials [25]. Figure 2 depicts the microstructure of a porous Ti scaffold [32].

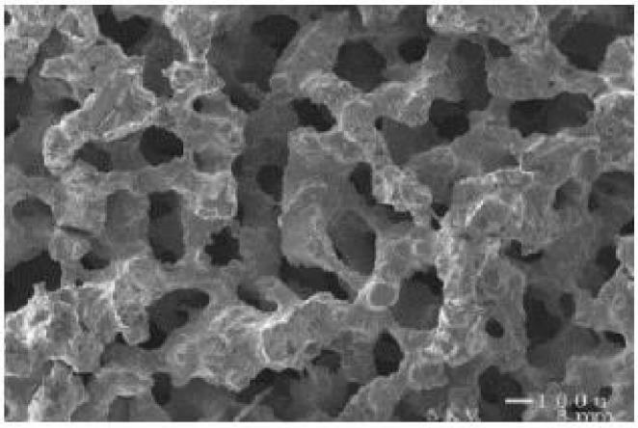

Figure 2: SEM micrograph of Porous Ti [32].

For scaffolds, significant porosity is needed to permit for tissue conduction; nevertheless, a combination with mechanical strength should be established.

2.1.3 Biomedical Titanium Alloys

Titanium alloys possess significantly less Young's moduli (55–110 GPa) than 316LSS (210 GPa) and Co–Cr alloys (240 GPa). The figure 3 depicts the elastic moduli of several biomedical titanium alloys as well as bone. They do, meanwhile, contain moduli that are much greater than bone (10–30 GPa). Because of the large disparity in moduli between such implants and the surrounding bone, bone resorption occurs all around implant, causing implant loosening and, as a result, the sufferer might undergo severe reoperation. The "stress shielding effect" refers to this biomechanical mismatch. As a result, implant materials must have a modulus similar to bone they restore so as to minimize stress shielding effect. This eventually led to growth of novel forms of Ti materials for implant (containing design plus fabrication) with lower modulus similar to those of bone, thru goal of achieving reduced stiffness and sacrificing other important parameters [33-37]. Several low-moduli, non-toxic β-type titanium materials for implants, like Ti–24Nb–4Zr–8Sn (Ti2448) [38] and Ti–29Nb–13Ta–4.6Zr (TNTZ) [33], have indeed been

produced. Other option is utilizing porous structures rather than solid materials since porosity may lower the both modulus as well as weight of material when compared to solid alternatives. Additionally, modulus of a porous material may be conveniently adjusted, and bone cell in-growth might be enhanced over solid equivalents [39-43]. As a result, porous materials can be used in joint replacement surgery as well as bone grafting application [44].

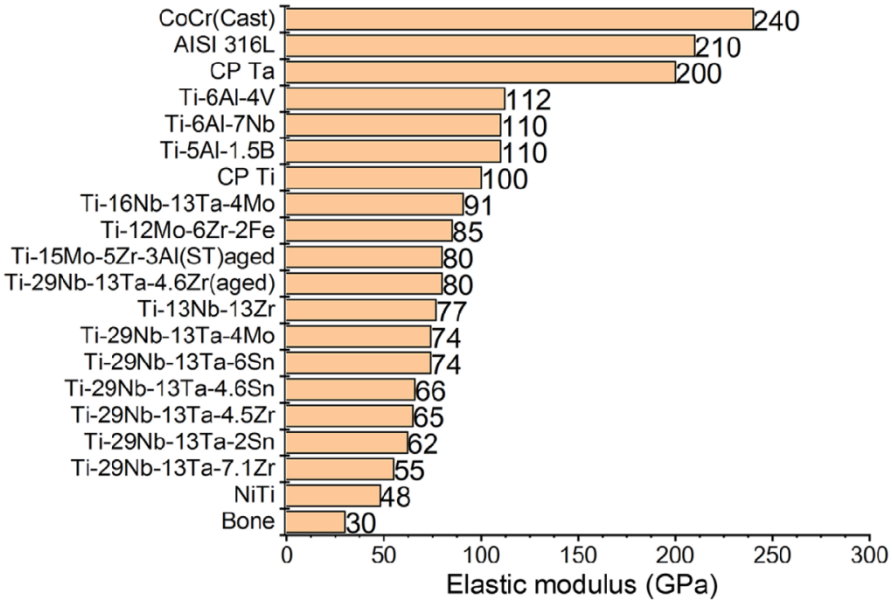

Figure 3: Elastic moduli of different biomedical alloys and bone [45].

2.2 New Preparation methods for Ti alloys for biomedical application

Several processing procedures, including as casting, powder metallurgy, forging and sintering, were used in fabrication of Ti alloys. Because these standard procedures have recently been detailed in detail, only several innovative Ti alloy production methods for biomedical applications were described here.

2.2.1 Selective Laser Melting

Biomedical implants frequently possess complicated contours and dimensions that vary depending on the patient. As a consequence, traditional technologies are often associated with substantial time, material, and energy prices when producing biomedical implants. SLM, one of the AM methods, has indeed extensively being used in recent years to tackle the traditional

production challenges of Ti-based materials [46-50]. SLM technique is layer-by-layer technique performed in a restrictive environment in conformity with a pre 3D model. Ti alloy pieces were created layer - by - layer by selectively melting material at fast pace utilizing a computer-controlled laser [46]. SLM has a number of benefits over traditional fabrication, including shorter production times, stronger material usage, nearly no geometric constraints, and additional post-processing [51]. SLM-produced alloys exhibit unique microstructures when compared to traditional equivalents owing to quick heating/cooling rate in SLM treating [52, 53]. The (α+β)-type Ti–6Al–4V alloy generated by SLM possess dominating fine acicular α' martensite long with certain previous β grains, whereas standard Ti–6Al–4V alloy (Grade 5) has a distinctive equiaxed α+β microstructure [51].When contrasted to traditional analogues, SLM-produced Ti–6Al–4V has equivalent or else higher mechanical qualities because of its unique microstructure. SLM studies on (α+β) type Ti alloys were too conducted upon Ti–6Al–7Nb, that have superior mechanical characteristics, resistance to corrosion, and biocompatibility [54]. SLM-produced Ti–6Al–7Nb, like Ti–6Al–4V, has predominantly α martensitic plate [55]. Because powder feedstock β-type Ti alloys are not accessible towards SLM, very few SLM research was done on β-type Ti alloys. Present investigation team investigated SLM upon β-type Ti–24Nb–4Zr–8Sn alloys [56, 57].

Having the use of biomedical implants inside the human body in mind, the current research team contrasted the corrosion behaviour of SLM-produced Ti–6Al–4V in 3.5 wt. % NaCl solution to the commercialized Grade 5 alloy [58]. Electrochemical studies revealed that passive current density of SLM-produced Ti–6Al–4V alloy (0.841±0.0275 μA cm^2) is twice that of commercial Grade 5 alloy (0.390±0.0125 μAcm^2), and the fitted film resistance of industrial Grade 5 alloy (94±7 kV cm^2) is likewise twice that of SLM-produced Ti–6Al–4V (40±6 kV cm^2). The findings suggest that SLM-produced Ti–6Al–4V has worse resistance to corrosion as commercial Grade 5 alloy, owing to a comparatively significant quantity of acicular α' martensite and smaller amount of β-Ti phase in the microstructure of SLM–produced Ti–6Al–4V [58]. Despite heat treatment to remove the acicular α' martensite in SLM-produced Ti–6Al–4V, the corrosion resistance of heat-treated SLM–produced Ti–6Al–4V was not enhanced [59]. In simulated bodily fluid, however, SLM-produced Ti–TiBbiocomposite demonstrated greater corrosion resistance than traditional equivalents [60]. All of the variations in corrosion behavior among SLM-produced Ti alloys and

traditional Ti alloys may be attributed to variances in microstructures caused by process parameter. Furthermore, there is very little research on the corrosion behavior of SLM-produced Ti alloys (as well as other materials like Al alloys as well as stainless steel), so further research is required to fully comprehend the corrosion behavior of SLM-produced alloys. While SLM is frequently utilised to examine the process and mechanical characteristics of titanium alloys (particularly Ti–6Al–4V alloy), the existence of α' phase in the microstructure of SLM-produced Ti–6Al–4V has led in the alloy having poor service qualities. Latest studies have sought to eliminate the existence of α' phase in SLM-produced titanium alloys.

2.2.2 Electron Beam Melting

Other common metal additive manufacturing process, electron beam melting (EBM), is regarded as a breakthrough industrial production technology for producing biomedical Ti alloys [61]. EBM technology, like SLM, employs a layer-wise processing approach that employs a high-energy electron beam as a heat source to produce alloy components on a powder bed depending on a computer-aided design (CAD) model. Metal components with complicated forms may be swiftly prototyped using EBM with few processing steps [61]. In contrast to SLM technology, the EBM process is carried out in a vacuum atmosphere and may warm the powder utilised, resulting in alloy components with greater densities [62]. With an industrial standpoint, EBM is a fantastic alternative method for producing biomedical Ti alloys.During EBM procedure, the electron beam travels quickly and melts the powder to produce a molten pool in a vacuum condition before solidifying the melt. As a result, the solidification of building layer has an effect on the constructed layer underneath. The total temperature of a constructed item is kept high because to the poor cooling rate & heat buildup throughout the EBM procedure [61]. These process properties result in a different microstructure in EBM alloys when matched to SLM and traditionally manufactured analogues. [63].

EBM has indeed been extensively employed in synthesis of Ti–6Al–4V to date. Irrespective of the significant variation in microstructural fineness, both EBM-fabricated Ti–6Al–4V as well as wrought Ti–6Al–4V exhibit a basket-weave microstructure having columnar previous β grains delimited thru grain boundary [64]. Through an EBM-fabricated Ti–6Al–4V, previous β grains contain a high <001> textural element along build direction [65]. The corrosion tendency and

current of EBM-fabricated Ti–6Al–4V are somewhat greater and marginally lower than wrought Ti–6Al–4V, showing moderately improved resistance to corrosion in phosphate buffered saline [64].The justification for this is that the EBM-fabricated Ti–6Al–4V has greater proportion of β phase as well as substantially refined lamellar α/β phases than wrought Ti–6Al–4V. Corrosion performance of EBM-produced Ti–6Al–4V is superior to that of SLM-produced Ti–6Al–4V. Such variation is due to differing phase elements of EBM-fabricated Ti–6Al–4V as well as SLM-fabricated Ti–6Al–4V [66]. It's expected that corrosion behaviour of monolithic phase Ti alloys will be considerably identical regardless of the production processes used.

2.2.3 Preparation methods of porous Ti alloys

Despite contemporary Ti alloys could handle the majority of biomedical usage difficulties; its elastic moduli still are larger than even human bones. Newer Ti alloys having reduced moduli are predicted to decline stress shielding effect. In addition to expansion of novel low-moduli β-type Ti alloys, porous Ti alloy structures possess less moduli over their bulky equivalents. As a result, numerous experts have been working on producing porous Ti alloys in latest days. Porous Ti alloys with suitable macro or micro-pores regarding bone cell ingrowth as well as vascularization possess elastic moduli that may be modified over a large range [67, 68]. Though porous metals with larger porosities might enhance bone cell regeneration, the porous structures had the inverse result on mechanical qualities. As a result, balancing the porosity of porous metal components for bone ingrowth and mechanical characteristics is critical. As a result, techniques for producing porous Ti alloys having adequate potency which was actively researched [67, 69].

Ti alloy components with complicated forms may be produced using both SLM and EBM processes [56]. Porous Ti alloy scaffolds having nearly full density may be manufactured via pre-designing 3D models and tweaking factors [70]. Owing to its differences in structure and scanning compared to solid Ti alloy components, porous Ti alloy components possess reduced melt pool owing to lower input energy intensities required for higher density. Existing study examined microstructure as well as characteristics of rhombic dodecahedron Ti–24Nb–4Zr–8Sn scaffolds having porosity of 75% fabricated using EBM and SLM techniques. Spot size of laser (40 mm) is substantially lower than electron beam spot size (200 mm), resulting in reduced melt pool for SLM than for EBM. Furthermore, as illustrated in Figure 4, the SLM as-produced

surface having 50 mm layer width is smooth than of EBM having 70 mm layer thickness. Similarly, the mechanical characteristic of scaffolds with same structure varies slightly [62].

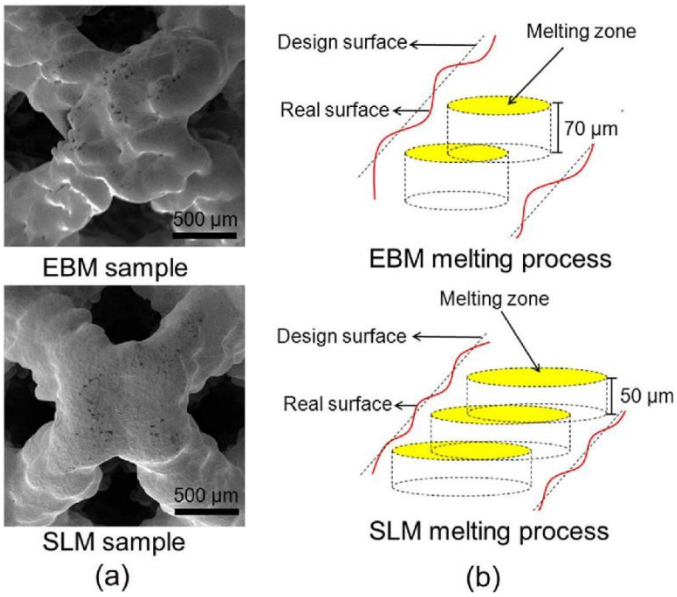

Figure 4: a) SEM figures illustrating surface characteristics of rhombic dodecahedron structural Ti–24Nb–4Zr–8Sn scaffolds generated by EBM and SLM, and b) melting schematic diagram [62].

SLM-fabricated Ti–24Nb–4Zr–8Sn components have modestly lesser elastic modulus (~0.95±0.05 GPa) and a greater compressive strength (~50 MPa) to EBM-fabricated Ti–24Nb–4Zr–8Sn (~1.34±0.04 GPa; compressive strength: ~45 MPa). Heat treatment might reduce this disparity. Moreover, Liu and team [49] explored mechanical behaviour of 75 % porosity SLM-fabricated porous Ti alloys utilising cubic, topology optimised, or rhombic dodecahedron structures, and findings disclosed that such 3 structures seemed to have various local stress concentrations and stress distributions throughout distortion, resulting in difference in absorption of energy.

Traditional sintering of Ti besides related alloys necessitates higher temperature (1200–1400 °C) in higher vacuum condition for an extended period of time (24 to 48 h), resulting in detrimental alterations in morphology as well as mechanical characteristics of sintered products [71]. Spark plasma sintering (SPS) that uses external current for assisting powder consolidation, has subsequently received a lot of interest [72]. The powder is sintered using this approach in a high

electric field, a stress field, plus a lower sintering temperature. It possesses benefit of having a quick heating/cooling rate plus combining sintering and heat treatment [73]. As a result, SPS technology may effectively conserve energy while sintering the powder utilised. Recent research on the preparatory work of porous Ti alloys via SPS focuses primarily on reduced temperature and reduced pressure situations which could certainly sinter Ti and its alloys into powders [74], since higher current discharges yields ionisation in plasma, which could melt local oxide film upon particle surface and permit creation of junctions among particles. Porous CP–Ti generated at 700 °C for 8 minutes below 50MPa via merging SPS with a NaCl dissolution procedure (NaCl could be simply separated through dissolution in water) demonstrated yield strength ranging from 27 to 94MPa and elastic modulus ranging from 6.2 to 36.1GPa, indicating a densely connected structure with homogenous distribution of pores [75].

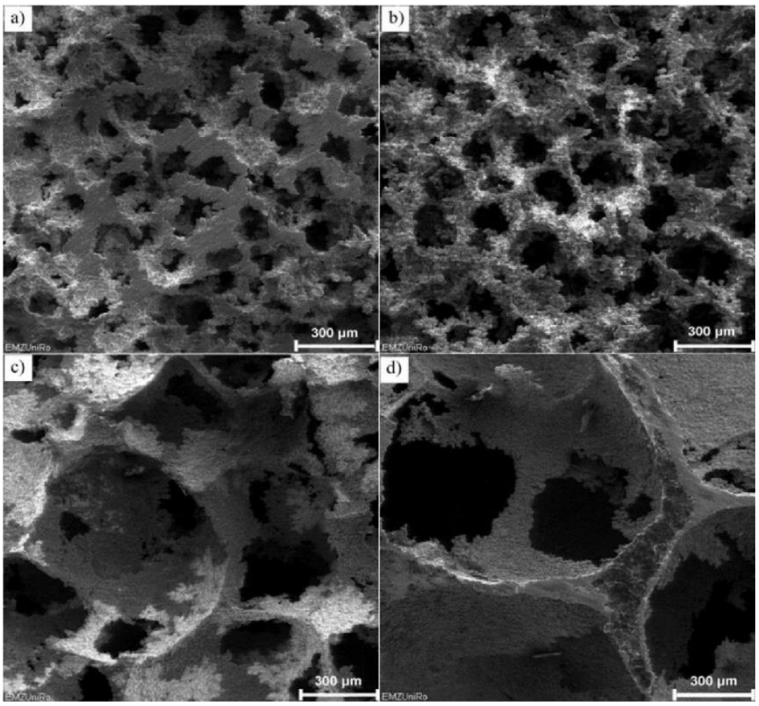

Figure 5: Characteristic porous CP–Ti microstructures having a porosity of 55% and varying pore sizes: a) 125mm, b) 250mm, c) 400mm, and d) 800mm [75].

Figure 5 [75] depicts conventional morphologies of porous CP–Ti having porosity of 55% although varying pore diameters. Porous Ti–5Mn also was created by mixing the SPS approach using ammonium hydrogen carbonate and blowing agent TiH_2 at lesser-pressure conditions at various temperatures for nearly 5 minutes [76]. Porosity of produced porous Ti–5Mn decreased

from 56% to 21% as sintering temperature climbed from 950 to 1100 °C, whereas the elastic moduli climbed from 35.0 to 51.8GPa [76]. Furthermore, SPS may generate a field effect among powder particles and successfully limit grain formation during sintering, making it a nanostructured/ultrafine-grained material forming method [77]. As a result, SPS offers a unique way for producing nanostructured/ultrafine-grained Ti as well as Ti alloys for biomedical purposes.

2.3 Selective Laser Melting (SLM) Process and Processing Parameters Involved

Conventional subtractive fabrication techniques are essentially material exclusion procedures that are managed by eliminating unwanted layers of material for generating product having a desired profile. In contrast to subtractive production methods, evolving innovative additive manufacturing techniques such as SLM are a layer-by-layer procedure wherein components are generated layer - by - layer via preferentially full melting and realigning starting powder utilizing a computer-based laser beam in shielding atmosphere. The SLM method begins with the creation of a 3D model of product utilizing computer assisted design (CAD) software, which is then accompanied by mathematically cut thin layers. The thin layers were then transported to specialized SLM equipment for materializing finished product layer by layer.

Following that, a substrate is placed and flattened on build platform in preparation for component manufacture. Loose thin layer powder having thickness equal to sliced layer width is put upon build substrate. The powder bed is scanned and treated utilizing pre-defined production variables and patterning based upon pre-designed CAD model. Following the manufacture of the first layer, then procedure is reiterated for subsequent layers till entire component is built [78]. The phrase "selective" refers to the processing of only a portion of the powder. The keyword "laser" indicates that a laser is used for treating, while the word "melting" indicates that a certain powder is totally melted. One monitoring computer system, a treatment laser, an automated powder feeder container, and major accessorial elements (for example, inert gas system protection, roller/scrapper, and overflow container) are often included in an SLM system [78]. SLM has a number of benefits over traditional production technologies, comprising near-net-shape fabrication, shorter fabrication times, higher material usage, and essentially no

dimensional limitations, allowing it to harvest intricate-shape components practically without the requirement for supplementary post-processing.

2.3.1 Process Parameters Involved

The basic goal of the SLM method is to produce components having full density and devoid of flaws. It is difficult to achieve this aim as there is no mechanical pressure throughout SLM that is primarily defined by gravity and capillary forces, as well as heat effect. Because SLM involves a vast number of processing factors, proper management of the corresponding parameters results in a high-quality output. Some characteristics (like laser wave length and laser operating mode) are fixed and regulated by the SLM device. Furthermore, certain characteristics of the powder employed (like viscosity and heat conductivity) are fixed, defining the boundary constraints of the SLM procedure. Some characteristics, such as manufacturing or process conditions, on the other hand, must be computed and optimised with caution [79]. Generally, the laser energy density, *E*, supplied to a certain volume of powder material via SLM for a particular material is given as: $E=P/(v.t.s)$.

Where *P* is the laser power (W), *v* is the scan speed (mms^{-1}), *t* is the layer thickness (mm), and *s* is scan spacing (mm). The laser energy density is determined by such critical parameters for densification and precision of SLM-fabricated components, which determine their attributes. Seen in the previous equation, raising laser power and/or reducing scan speed, layer thickness, or scan spacing will indeed boost laser energy density and hence powder temperature. A greater incoming laser energy density causes more melting and hence a larger final density. Because the development of a totally molten state is necessary for producing fully dense objects, a large laser energy density delivered to powder materials is required. Generally, to generate components with maximal density, a specified minimum laser energy density is necessary. [51].

Figure 6 depicts a layout of various SLM processing [80] settings. The laser beam passes over the powder bed at a consistent speed termed as scan speed (v) during SLM that regulates the duration of manufacturing. In other words, if manufacturing time is limited, faster scan rates are necessary. With raising scan speed, meanwhile, the maximum laser power of a certain SLM device must be considered. The quantity of energy and time needed to melt/consolidate a layer of

powder is defined by layer thickness (*t*). Layer thickness is critical because adequate connection between layers could only be achieved by re-melting previously treated layers. When the layer thickness is increased, the production time is lowered. Nevertheless, larger energy input is necessary to thoroughly melt dense layers that might result in increased surface roughness and decreased precision. Scan spacing (*s*) is commonly selected as parallel lines in SLM and is hence also known as "hatch space." According to [51], scan spacing controls the overlap of neighboring solidified tracks, which has a major impact on the porosity and surface roughness of SLM-produced components. The scan spacing must be meticulously set to insure that neighboring tracks link well. As a result, it should range from half and full width of melt pool.

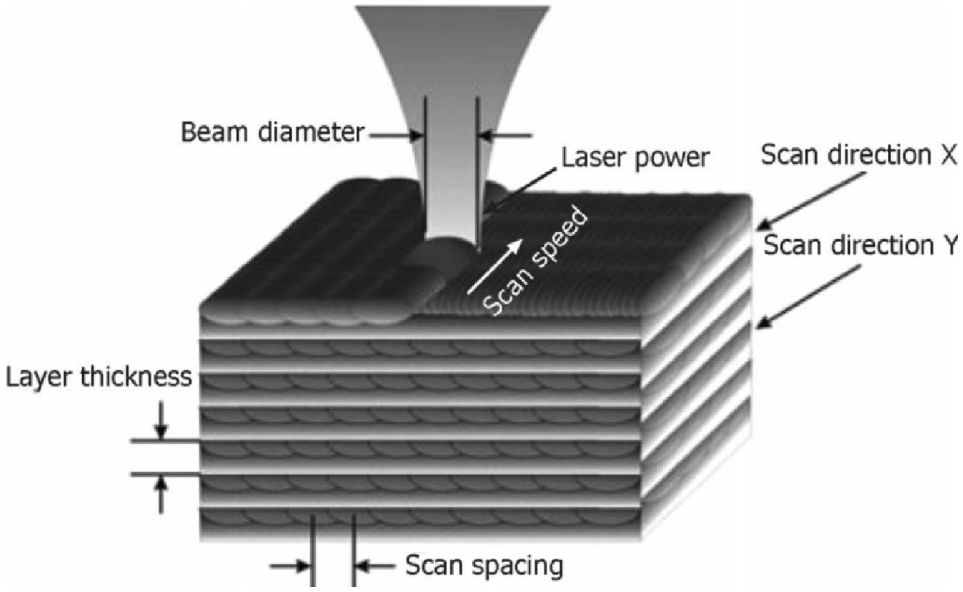

Figure 6: Schematic of selective laser melting (SLM) parameters [80].

Other key characteristics (often known as "scanning strategy") in the SLM procedure include the length and pattern of laser scanning vectors. The geometry of scanning determines the length of the scanning vector. Such scanning, termed as a "manufacturing pattern," can be done in a variety of methods. The laser scan pattern is normally composed of parallel and straight lines, with the option of circular or spiral coverage. The scanning pattern's direction can be modified inside a single layer or between successive layers. The first two versions (Figures 7 a–b) are known as uni- and bi-directional (zigzag) scanning patterns, correspondingly. In addition, the scanning direction could be rotated from section to section, as illustrated in Figure 7c for island scanning (inter-layer). The scanning direction could also be adjusted across subsequent levels

using varying degrees (Figure 7d). The design of the production pattern has an impact on the quality of the SLM-processed item.

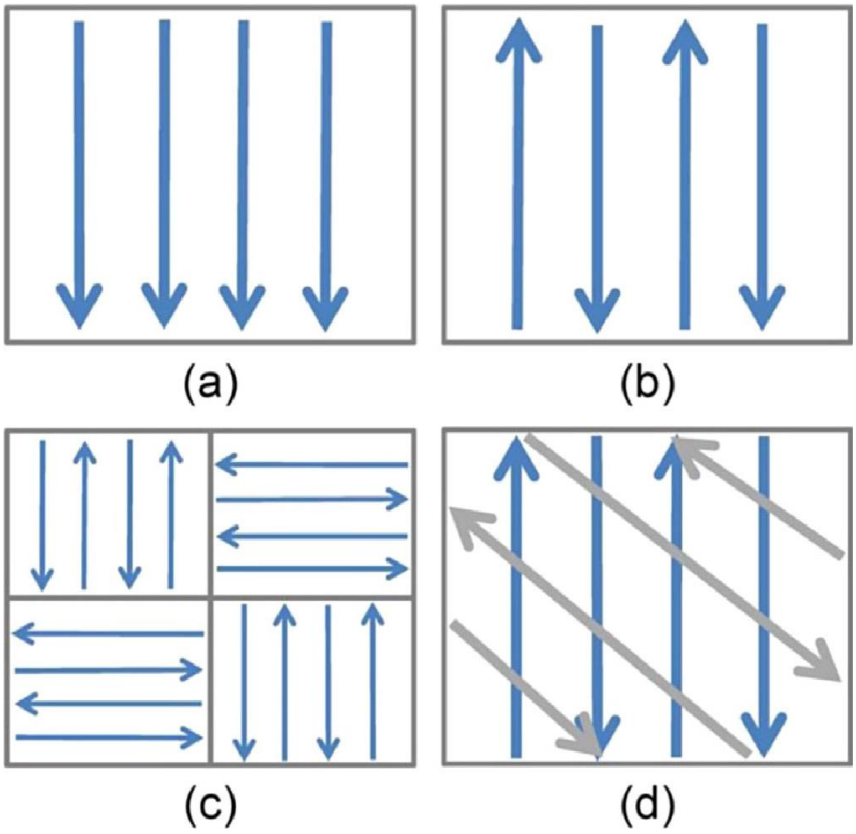

Figure 7: Different SLM processing patterns: (a) Uni-directional scanning, (b) Bi-directional scanning (zigzag) scanning, (c) Inter-layer scanning, and (d) Interlayer rotation scanning [51].

2.3.2 Needs of Developing New Alloy Powder Materials for SLM

The SLM technique must engage with certain powder, laser, and scan factors that have an impact on the density, surface quality, microstructure, and consequent qualities of the SLM-produced samples. Heat energy drives the melting/consolidation of metallic powder during SLM, and the temperature could rise to evaporation temperature. As a result, the qualities of the starting material, and also particular powder properties, are critical for the creation of a melt pool and laser absorption. For instance, the powder's features (ie, kind, shape, and size) and qualities have a major impact on the SLM process, powder flowability, and laser-powder interaction. Because

SLM uses powder as the beginning material to make components, the shape of the starting powder might influence the density and quality of the final SLM-processed items. Powder morphology describes how tightly packed the particles are when a fresh layer of powder is placed on top of a formerly established solid layer. As a result, powder morphology is an important component in determining layer thickness and surface roughness throughout the SLM process. Powder morphology is concerned with the form and size of powder particles and is heavily influenced by powder manufacturing procedures. Powder materials having a spherical form are appropriate for SLM. Atomization is commonly used to create spherical powder materials. Consequently, the chemical compositions of feedstock powder for SLM are quite limited. Just 29 typical metal powder materials are now accessible for SLM, with only CP–Ti, Ti–6Al–4V, and Ti–6Al–7Nb obtainable for titanium alloys [81]. As a consequence, reduced price, lesser spherical powder materials for SLM are required. As one of the low-cost and powerful techniques to modify powder mixture, ball milling (or mechanical alloying) might be an alternate technology for creating near-spherical powder materials for SLM. Powder materials that have been ball-milled have been effectively employed for subsequent powder consolidation into bulky samples. Long-term ball milling, on the other hand, is said to produce irregular-shaped powder particles that generate less compaction, resulting in enhanced porosity.

2.3.3 Defects and Unfavorable Issues in SLM

Because SLM is a complicated metallurgical procedure, optimizing all of the aforesaid connected process variables is required for SLM to produce high-density and high-quality parts. Owing to inappropriate powder bed density and reduction in solubility of certain elements in melt throughout solidification, imperfections like unmelted regions and porosity may be formed through SLM owing to inadequate powder bed density and reduction in solubility of certain elements in melt throughout solidification [79].

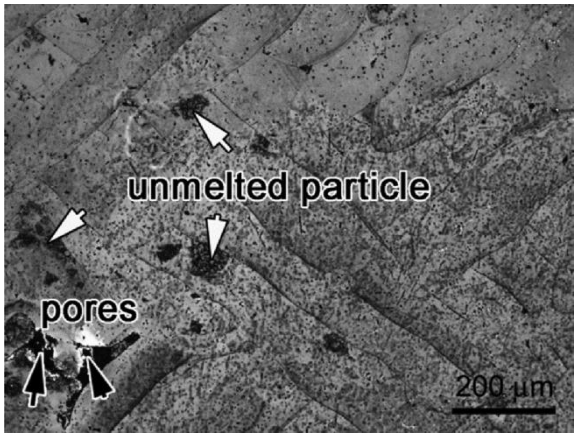

Figure 8: Optical microstructures of the SLM-produced Ti–24Nb–4Zr-8Sn part, showing porosity and un-melted areas due to improper SLM processing parameters [79].

Figure 8 exhibits typical porosity and unmelted regions caused by poor processing settings in a β-type Ti-24Nb–4Zr–8Sn sample during SLM processing [79]. These flaws might be reduced or eliminated by adjusting the processing settings. Owing to localised abnormalities caused by balling effect, fractures, heat affected zone (HAZ), ambient circumstances, and residual stress, unfavourable problems and flaws may arise in SLM-produced components. It is critical to look at these difficulties in order to increase the quality and longevity of SLM-processed components. The balling effect is the fragmentation or droplet formation caused by capillary instability in a melt pool [82]. Boosting scan speed might have an influence on melt pool stability since it might induce "balling effect" in the extended liquid pool. The balling effect is a complicated physical metallurgical phenomenon that occurs as an undesired consequence during laser-based processing. Generally, laser scanning occurs line by line during SLM, and laser energy promotes melting in powder particles across a row, resulting in the production of a continuous liquid track with a cylindrical shape. The drop in surface energy of the liquid track may continue till the cylinder breaks apart in order to attain ultimate equilibrium, resulting in the production of many metallic agglomerates of spherical shape termed as the balling effect (Figure 9) [83].

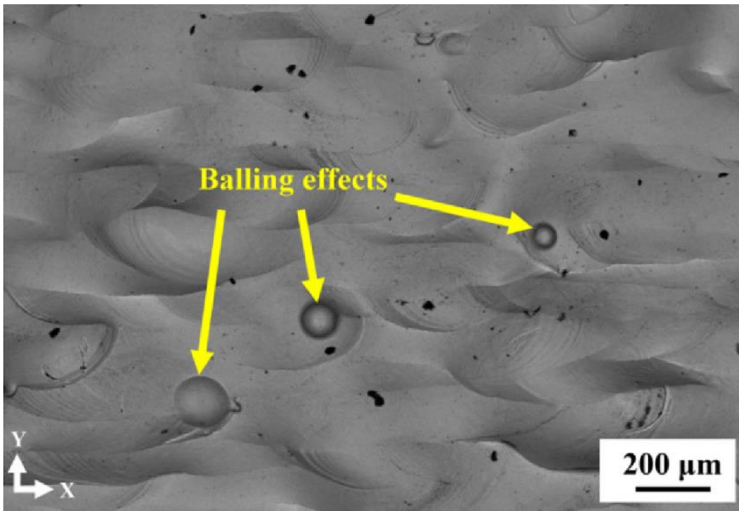

Figure 9: Scanning electron microscopy (SEM) image showing balling effect in SLM-processed CP–Ti [83].

During track processing, the balling effect could result in the creation of weak interline bonding. Furthermore, the balling effect is a specific weakness that is harmful to the homogeneous deposition of the next layer of powder on the previously treated layer that might lead to porosity and delamination due to the combination of poor interlayer bonding and thermal stresses. Balling effect could be prevented if the melt pool's stability is enhanced by lowering the length-to-width ratio and/or increasing the contact width. Greater laser power or a slower scan speed, for example, could be used to accomplish this. The balling effect is affected by the kinematics of the breaking procedure. When the time required for break-up is greater than the time required for solidification, no balling effect occurs.

2.3.4 SLM produced Ti based materials

Titanium materials are attractive candidate materials for SLM because they are costly and difficult to prepare to utilize traditional processing processes. End-user benefits like net form capability for complicated shapes, excellent material usage, and minimal machining make SLM an appealing solution for producing titanium components, particularly those with complex shapes. Ti–6Al–4V titanium alloys have been the most popular and commonly utilised titanium alloys for SLM research. Significant efforts were undertaken to investigate several facets of this alloy's SLM, namely densification behaviour, microstructure, and mechanical characteristics

[51]. Furthermore, SLM of additional (α+β)-type titanium alloys, such as Ti-6Al-7Nb, has been investigated [84]. Along with Ti–6Al–4V and Ti–6Al–7Nb, β-type titanium alloys (like Ti–24Nb–4Zr–8Sn and Ti–21Nb–17Zr) have been also studied [79]. β-type titanium alloys have a lower Young' modulus, that minimizes the stress shielding effect and makes them suitable for biomedical purposes. Furthermore, the densification, microstructures, and mechanical characteristics of CP-Ti have recently been studied [83].

2.4 Human Bone

It is necessary to comprehend the form and characteristics of bone in order to create scaffolds that substitute bone. Bones contain immensely complicated structures made up of bone mineral and an extracellular matrix (ECM) [85]. Bones perform a variety of tasks, including bodily movement facilitation, muscle attachment sites, and soft tissue support structures [85]. Bone is a natural material combination with anisotropic properties and a seven-tiered structure [85]. Figure 10 depicts a basic layout of this arrangement, which may be observed in most regions of the body.

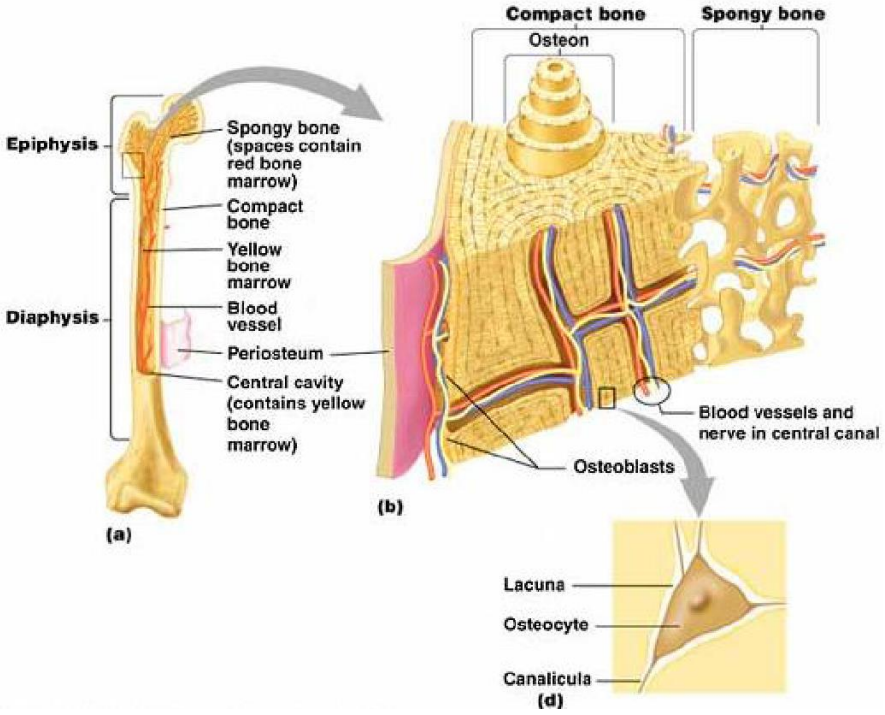

Figure 10: Human Bone Structure [85].

The cortical region accounts for 80 percent of bone, whereas the cancellous or spongy trabecular zone accounts for the remaining 20 percent [85]. Because of these differences, the elastic modulus of bone ranges from 4 to 30 GPa [29]. The cortical zone's microstructure is defined as a thick solid, whereas the cancellous region is described as "a porous network of connecting rods or plates" [86]. Figure 11 depicts this permeable network. The difference in these two zones is caused by their respective densities or solid volume ratios. Cancellous bone has a density that is less than 70%, whereas cortical bone possesses a density that is more than 70% [85].

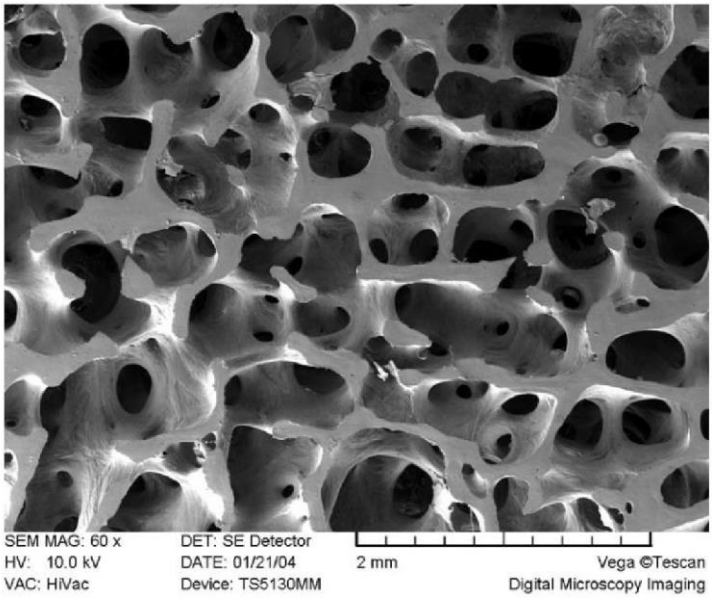

Figure 11: SEM of a 22-Year Old Male Human Bone [87].

Chapter 3

Material and Methodology

3.1 Powder Material

Ti-6Al-4V powders having spherical shapes and particle diameters lower than 90 m are employed as raw materials in the construction of the 15 mm cubic porous scaffolds structure. Ti-6Al-4V powders with chemical compositions conforming to ISO 5832–3 are produced using gas atomized technique, as stated in Table 4. As can be seen in Figure 12, SEM pictures of Ti-6Al-4V powders reveal that they are approximately spherical with a smooth surface that increases flowability in the SLM procedure.

Table 4: Chemical composition of Ti-6Al-4V powder.

Element	Ti (wt.%)	Al (wt.%)	V (wt.%)	Fe (ppm)	C (ppm)	H (ppm)	O (ppm)	N (ppm)
Mass	Balance	5.5-6.75	3.5-4.5	<3000	<800	<150	<2000	<500

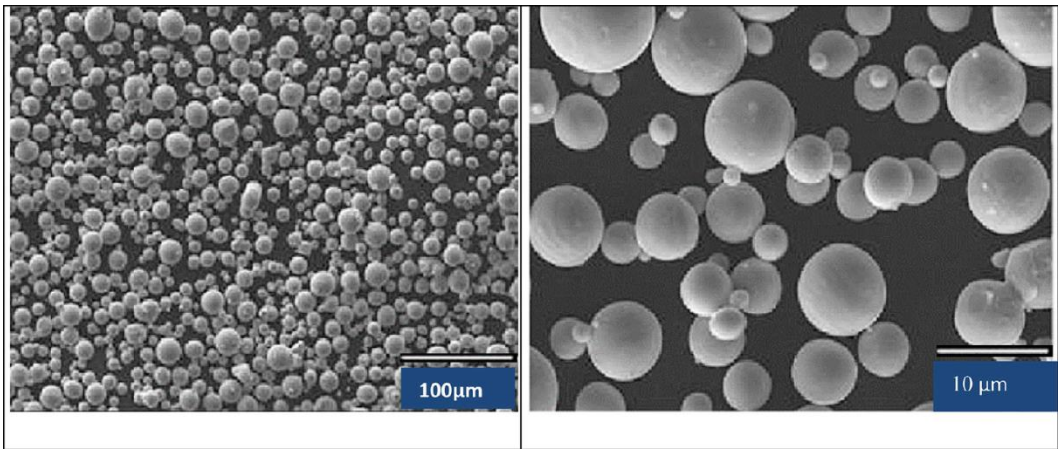

Figure 12: Image of Ti-6Al-4V powder of spherical shape.

The figure 13 depicts the particle size distribution determined using the Coulter Principle of laser diffraction. The powder is examined visually employing an optical microscope Olympus BX41 or GX51 (EOS, Finland) to explore powder monolayers and mounted, polished samples. Table 5 and Table 6 exhibit the results of this work's investigation of particle size distribution and powder characteristics.

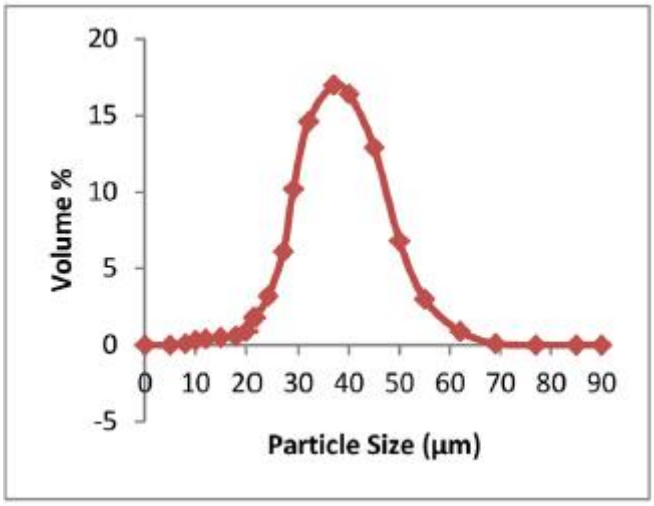

Figure 13: Particle size distribution of Ti-6Al-4V powder.

Table 5: Particle size distribution analysis.

Size Characteristics	Test Method	Result (mm)
d10	Laser Diffraction	29.48
d50		47.05
d90		71.92

Table 6: Powder property analysis.

Property	Test Method	Result
Apparent density	ASTMB212	2.42 gm/cm^3
Tap density	ASTMB527	2.9 gm/cm^3
Density	ISO3369	4.41 gm/cm^3
Water content	Karl Fischer titration	25.6 ppm

3.2 Modeling of Ti-6Al-4V scaffolds

By transferring data from 3D applications such as CAD, Rhino 6, and others, additive manufacturing (AM) technique is utilised to dramatically enhance the creation process of complicated structures with microscopic geometries. When compared to typical prototype manufacturing processes, it minimizes operating time and procedures by removing the mould building and casting process. As a result, AM technologies may dramatically minimize the time required to fabricate goods within an hour, as well as lower production costs, material waste, enhanced properties, and energy usage. AM techniques are capable of producing prototypes approaching net form based on 3D models where items are built layer - by - layer.Computer-generated 3D data is transformed to a standard tessellation language (STL) file type before being translated into numerous 2D cross-sectional layers via AM methods. AM methods then begin the process of creating a solid model by introducing materials from bottom layer to the top layer, as seen in Figure 14. Layer slicing is produced in a 3D printing bed for all printing samples at the same time (shown in Figure 15 and 16).

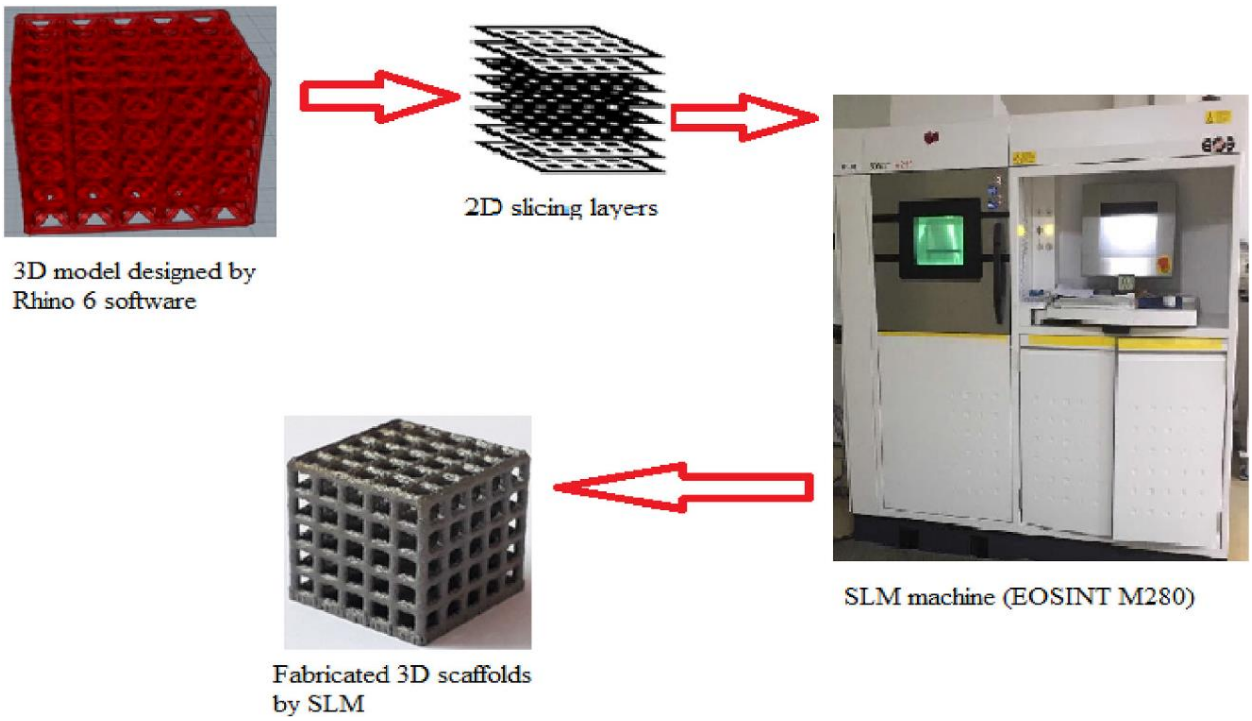

Figure 14: An overview of additive manufacturing process employed.

Rhino 6 software creates four alternative computer models for 15 mm cubic porous scaffolds (diamond, grid, cross, and vinties) with 65 % theoretical porosity. The model's theoretical porosity is computed by dividing the observed volume of the porous structure by the entire cubic volume.

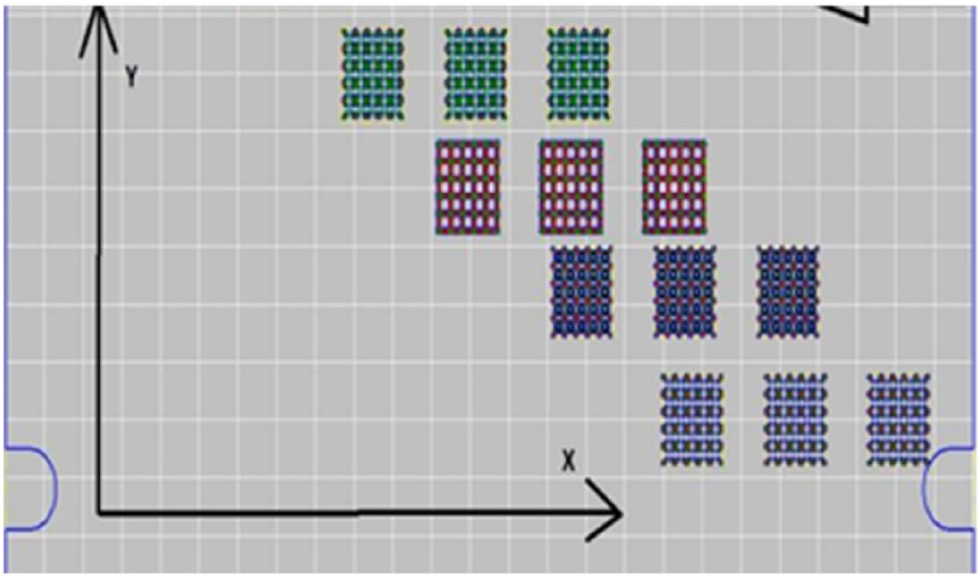

Figure 15: Computer layout of models on the machine bed.

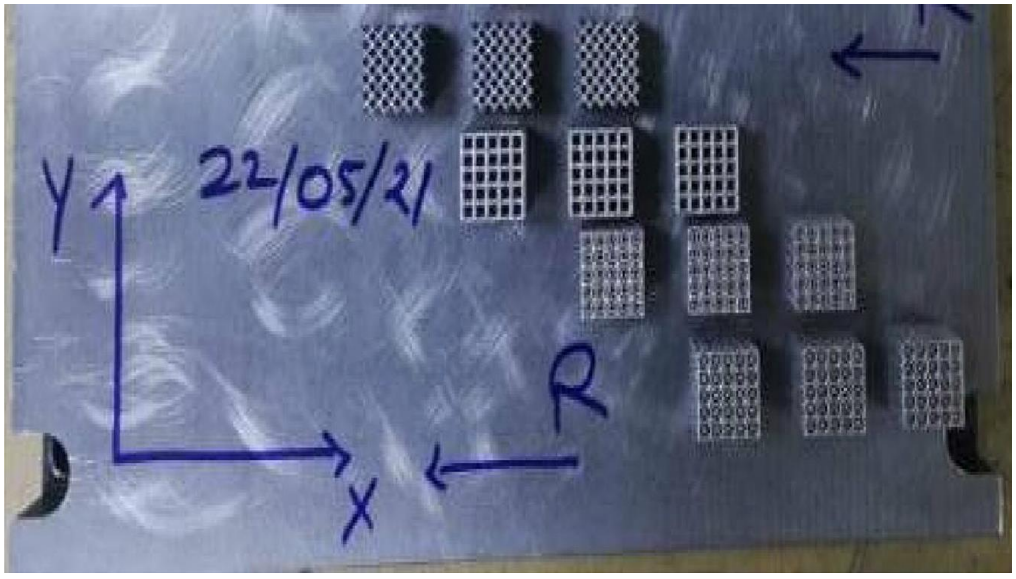

Figure 16: Actual picture of the manufactured samples on machine bed.

3.3 Fabrication of Ti64 scaffolds employing Selective Laser Melting

Selective laser melting (SLM) was first developed in 2002 as one of the ways for making complex components utilising metal additive manufacturing. This technique, which is already in its early phases of exploration, has indeed been utilised to produce bone supports and replacements in the biomedical industry. The method was initially investigated for the production of jaw and bone implants in the fields of dentistry and orthopaedics. Figures 17 and 18 show a standard SLM machine and procedure respectively.

Figure 17: EOS direct metal laser sintering machine (model: EOSINT-M280) installed at Central Tool Room and Training Center, Bhubaneswar, Odisha.

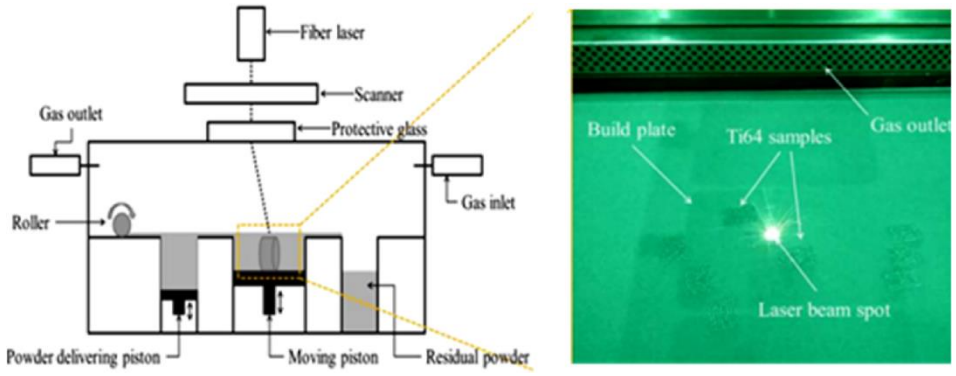

Figure 18. Schematic of typical Selective Laser Melting (SLM) process for fabrication of Ti64 porous lattice structures using SLM system EOSINT-M280.

Metal powders are used as the raw material in the SLM process, together with a laser, beam focusing setup, feeder mechanism, and build plate. SLM produces 3D metal components by fusing small metallic powders with the energy of a laser beam, specifically a Ytterbium fibre laser with wavelengths spanning from 1.06 to 1.08 µm and operating at 1 kW, as illustrated in Figure 19. A blade applies a layer of fine metallic powder to the construction platform, and the powders melt by laser beam into the 2D cross sections in an inert atmosphere that may be adjusted as needed. The galvanometer determines beam focus, whereas the F-theta lens governs beam movement. The constructing platform is then lowered to deposit another layer. This procedure will continue till the 3D section is done. The layer thickness might range from 15 to 150 µm.

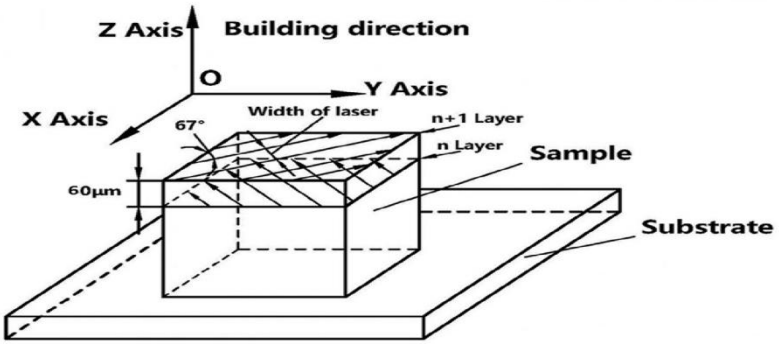

Figure 19. SLM manufacturing process.

The SLM machine (Model: EOSINT M280-400W) was used to construct all four samples, with input processing variables for TI-6AL-4V materials as indicated in Table 7.

Table 7: Input process parameters used in SLM process for Ti-6Al-4V.

Parameters	**Value**
Type of Laser	Ytterbium Fibre Laser
Shape of Spot	Spherical
Scan Speed (SS)	1000-1500 mm/sec
Diameter of Particle (PD)	>90 µm
Hatch Distance (HD)	0.02-0.14 mm
Power of Laser (LP)	225-475 W
Diameter of Laser (LD)	80 µm
Density (σ)	4.41 g/cm^3
Thickness of Layer (LT)	60 µm
Initial Temp. of Bed (Ti)	35 °C
Scan Angle of Rotation (θ)	67°
Building Space	200mm x 200mm x 200mm
Environment Maintained	Inert
Scan Path	“X" & Rotational

The SLM process is affected by variables such as material type, scanning, laser source, and ambient conditions. While the mechanical properties of the parts are highly impacted by porosity, a parametric analysis was undertaken for the chosen material to optimize the entire process, such as the density of parts. During procedure, four factors were chosen for experimentation: laser power, layer thickness, scanning speed, and hatch distancing. Ref. [88] determines the energy delivered by the laser beam:

$$E_d = \frac{P_l}{(v_s h t)} \tag{1}$$

Where E_d = energy density, P_l =laser power, v_s =scan speed, h = hatch distancing and t = layer thickness.

The energy density of the powder substance represents the amount of energy delivered per unit volume. The alteration of the input processing factors impacts the density and quality of the manufactured components as well as the volume energy density. The above equation indicates that greater energy induces increased melting, which reduces as layer thickness, scanning speed, and hatch spacing rise. To obtain great densification by totally moltening the powders, a high energy density is necessary. The SLM process's energy input is also impacted by procedure parameters and may be characterized as [89];

$$E_i = \frac{4P_l}{(\pi {d_l}^2 v_s)} \tag{2}$$

Where E_i=energy input, P_l= laser power, d_l =diameter of laser beam and v_s =scan speed.

Other measure is linear energy density (LED), which may be employed to quantify the energy input of powder material as [90].

$$LED = \frac{P_l}{v_s} \tag{3}$$

Where P_l=laser power and v_s = scan speed.

The porosity percentage (P) is affected by processing parameters such as energy density (E_d), scanning speed (v), laser power (P_l), and hatch distancing (h), and the correlation between them is as follows:

$$P = f\left(\frac{E_d v_s h^2}{p_l}\right) \tag{4}$$

The scanning speed (v_s), hatch distancing (h), and layer thickness all have a direct relationship with the layer thickness (t). The scanning speed and layer thickness are limited by the available laser power. The SLM process's construction rate is governed by the product of scanning speed, hatch distancing, and layer thickness and is stated as:

$$V_b = v_s h t \tag{5}$$

Where V_b is the construction rate (mm^3/s). In the current study, the scanning speed, hatch distancing, and layer thickness are assumed to be 1250 mm/s, 0.12 mm, and 60 m, correspondingly, with a maximum construction rate of 9.0 mm^3/s and a relative density of at least 99.98 %.

When compared to conventional processes such as casting and forging, SLM-fabricated parts offer great mechanical qualities, good grain refinement features, reduced phase segregation size, solid solubility, and chemical homogeneity. The melting characteristics of metallic powders are directly influenced by processing parameters such as scan line spacing, laser power, and scan speed. As a result, the process variables are closely monitored in order to produce high-quality biomedical equipment.

SLM is utilised in a range of industries, notably aerospace, automotive, and biomedical, to create complex patterns or lightweight structures. Because printed parts can have thin walls, deep gaps, and hidden channels, they are a promising way for creating porous scaffolds. Though bigger temperature gradients may generate residual stress, this may be prevented by post-heating the component adequately. Figure 20 depicts the SLM-fabricated Ti64 scaffolds.

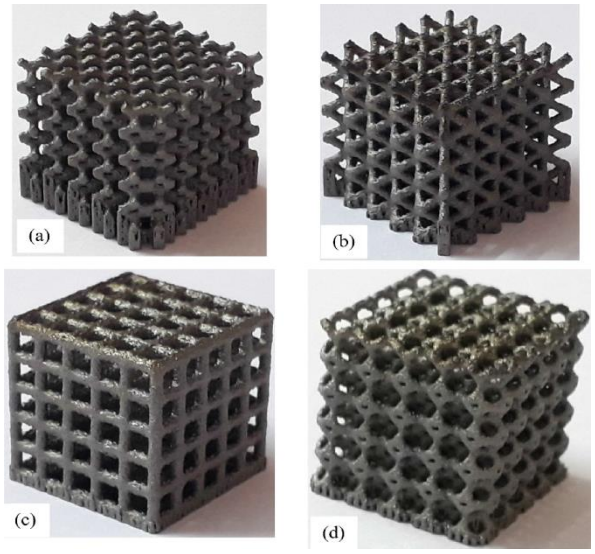

Figure 20: Fabricated Ti-6Al-4V porous scaffolds by SLM technique: (a) Diamond, (b) Cross, (c) Grid, (d) Vinties.

3.4 Heat Treatment Process

The specimens with the construction plate were heat treated after manufacture. The heat treatment modalities are as follows: (1) as-built SLM with no heat treatment and (2) annealed SLM with heat treatment at 900 °C for 120 minutes. The entire heat treatment procedure was carried out in an argon atmosphere at a rate of 5 °C/min, followed by cooling in the furnace. Table 8 shows the heat treatment technique used by SLM on as-built porous scaffolds.

Table 8: Heat treatment process of as-built scaffolds by SLM.

Sample	Temperature (°C)	Time (min)	Cooling
Diamond	900	120	Furnace cooling
Cross	900	120	Furnace cooling
Grid	900	120	Furnace cooling
Vinties	900	120	Furnace cooling

Chapter 4

Study of Mechanical Characteristics

4.1 Porosity

The density concept is used to calculate the porosity of the manufactured scaffolds. Every scaffold is submerged in a water-filled, finely graded measuring cylinder, and the amount of water displaced yields the volume of a porous scaffold. As illustrated in Figure 21, the porosity data is calculated by subtracting the volume of porous scaffold from the volume of dense scaffold. Table 9 shows the measured porosity value of each scaffold.

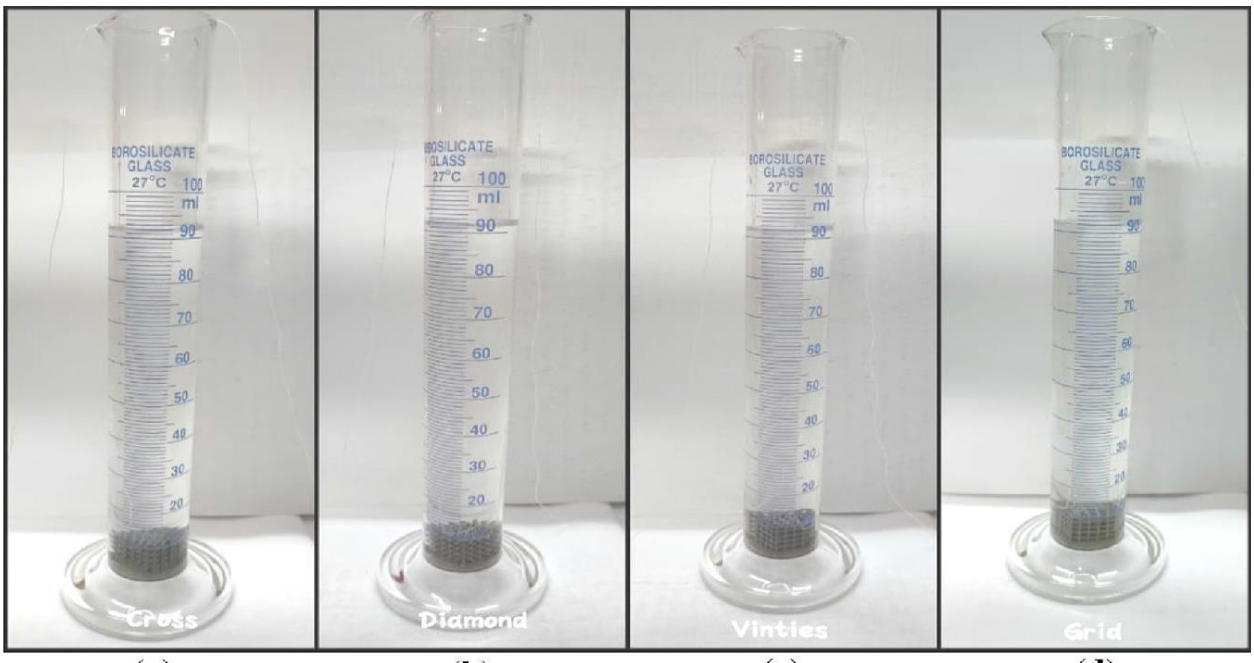

(a) (b) (c) (d)

Figure 21: Porosity measurement by measuring cylinder: (a) cross, (b) diamond, (c) vinties, (d) grid.

Table 9: Measured porosity of the fabricated scaffolds.

Sample type	Theoretical porosity	Measured Porosity		
		Sample 1	Sample 2	Sample 3
Diamond	65%	62.70%	62.60%	62.80%
Cross	65%	63.70%	63.80%	63.60%
Grid	65%	64.50%	64.50%	64.60%
Vinties	65%	64.40%	64.20%	64.30%

The grid scaffold has the highest percentage error porosity, while the diamond scaffold has the lowest porosity difference, as shown in Figure 22. The porosity of the manufactured scaffolds is smaller than that of the model scaffolds built with Rhino 6 software, as shown in Table 9 and Figure 21. The grid kind of sample has the lowest percentage of inaccuracy, whereas the diamond type has the greatest porosity difference. The grid-type sample might provide more similarities with the least amount of variation. The smaller range of real porosity can be attributable to the fact that the actual strut diameter of the mesh is printed somewhat larger during 3D printing because the metal powder is adhered to the wire surface. The porosity of manufactured scaffolds may be calculated as:

$$P = (1 - \frac{W_p}{W_d}) x 100\% \quad (6)$$

Where P = porosity, W_p = weight of the porous sample, and W_d= weight of the dense samples.

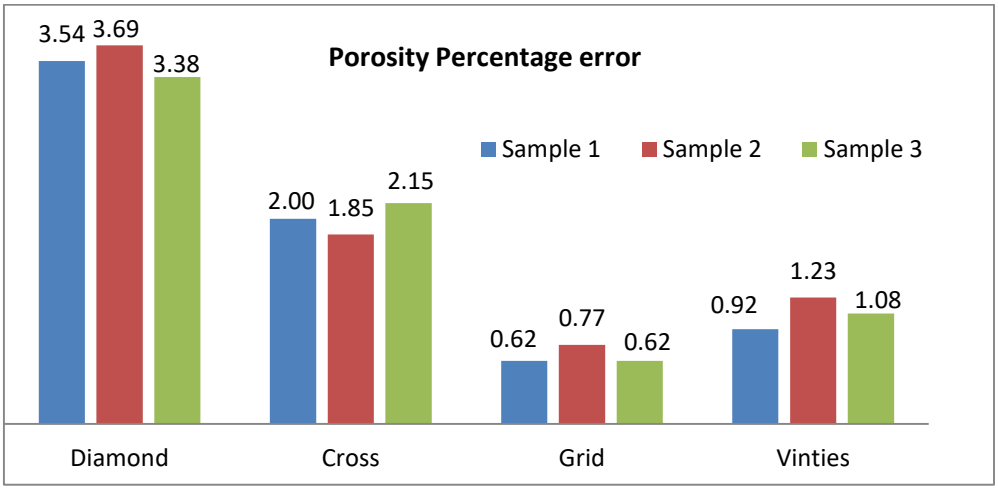

Figure 22: Porosity percentage error of scaffolds.

Apart from manufacturing process variables, there are a variety of scaffold design considerations which influence mechanical and biological qualities. Pore morphology, unit cell shape, and strut thickness are all things to think about. According to figure 23, the process parameters are the most critical factors influencing the porosity of SLM-fabricated samples.

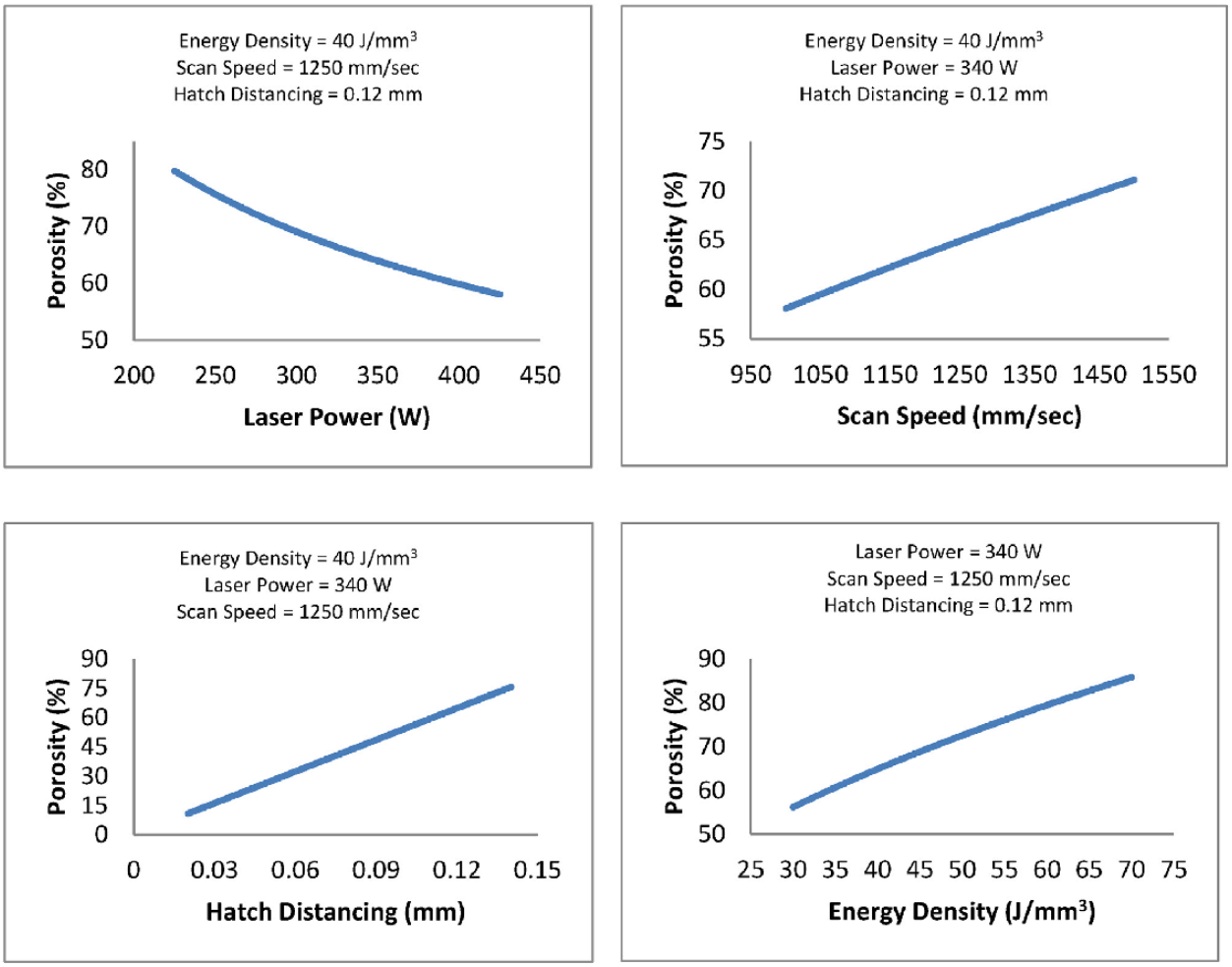

Figure 23. Effect of input process parameters of Ti-6Al-4V scaffolds during SLM.

4.2 Surface Roughness Test

Surface roughness is important in orthopaedic implants because it impacts both the implant and the bone tissue, and it can impede osteoblastic cell adhesion, proliferation, growth, and differentiation [91]. To achieve the desired roughness on implants, many procedures such as acid etching, sandblasting, and plasma spraying are used [92]. Metal powder-based methods are widely used to provide the appropriate surface roughness for osteointegration implants. In the SLM procedure, a large number of spherical Ti-6Al-4V particles are bound into the porous walls. The specimens are then heat treated at 800 °C for 2 hours in an argon gas environment, and microcavities develop on the walls, promoting interlocking with surrounding tissues once implanted in the human body. Absolute roughness levels (R_a) are important in the formation and development of human osteoblasts [93]. A result of less than 24.9 m R_a indicates a good effect. However, if the R_a value surpasses 56.9 µm, the impact is negative. It indicates whether or not to do additional surface treatments on items manufactured using SLM and EBM technologies.

The scanning electron microscope picture reveals that Ti-6Al-4V particles are approximately spherical having a smooth surface. The roughness value (Ra) of the prepared sample is measured with a Talysurf surface roughness tester (MITUTOYO SJ-210) and is displayed in the figure 24 and table 10. The grid type of sample has lower surface roughness.

Table 10: Surface roughness value (Ra) of prepared samples measured using Talysurf surface roughness tester.

Sample type	**Roughness value (R_a) in µm**		
	Sample 1	**Sample 2**	**Sample 3**
Diamond	46.2	49.6	52.2
Cross	43.7	41.8	45.7
Grid	23.2	21.6	22.2
Vinties	27.7	29.8	31.5

Figure 24. Talysurf surface roughness tester (Mitutoyo SJ-210).

According to the research [93], surface roughness has a beneficial impact when R_a is less than 25 µm and a negative effect when R_a is larger than 57 µm. Surface treatment is necessary if the roughness value is greater than 25 µm, and it is not required if the roughness value is less than 25 µm for an as-built implant. The measured R_a value of the four distinct types of constructed scaffolds shows that the grid scaffold has a R_a value less than 24.9 µm. As a result, grid scaffolds do not require further surface treatment. Excluding the grid sample, the other three versions require surface treatment based on the surface roughness test. The grid-type sample shows the minimum surface roughness, while the diamond-type sample exhibits a higher surface roughness value.

4.3 Compression test

The samples are evaluated in an INSTRON compression testing equipment to determine their mechanical characteristics. Because the sample is too tiny (15 mm cube), it cannot be accommodated in the INSTRON testing machine and may slip during the compression test. To prevent this condition and keep the samples securely held throughout the compression test, an extra attachment is devised with two 5-mm-thick HSS compression plates. Figure 25a depicts the upper plate, whereas Figure 25b depicts the lower plate. The primary goal of such plates is to

retain the sample and reduce the impact of scaffold compression. The scaffold is held in between the plates after attaching it to the INSTRON machine, as illustrated in Figure 26.

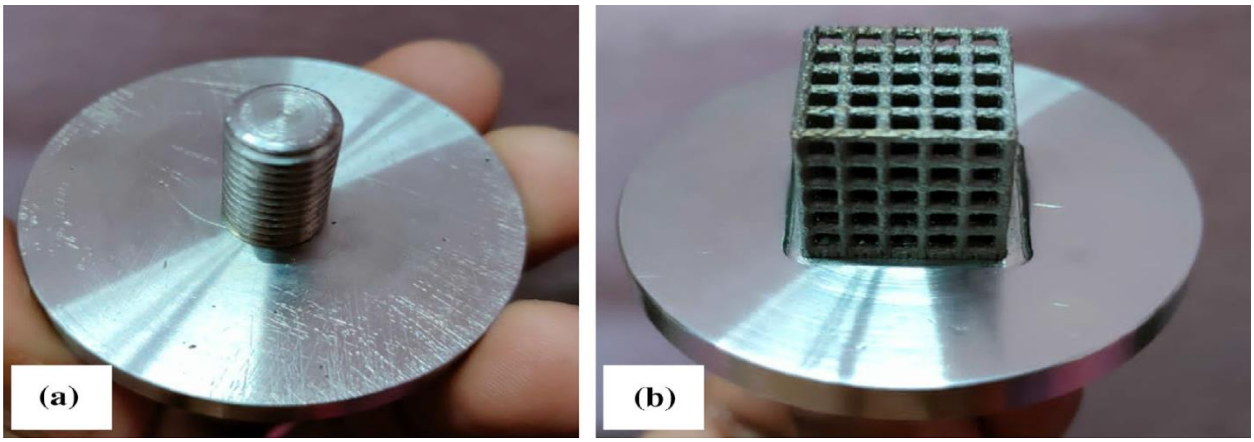

Figure 25: Upper HSS plate to be fitted in top part on INSTRON machine, b lower HSS plate where samples will be kept and to be fitted at the bottom part on INSTRON machine.

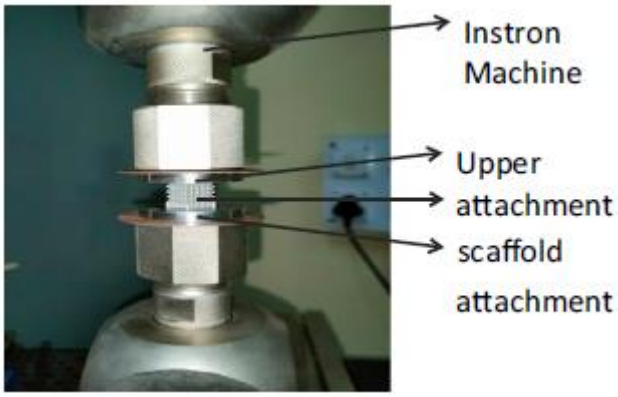

Figure 26: Sample held in INSTRON testing machine with two additional attachments.

Using an INSTRON machine having a maximum load capacity of 25 kN, uniaxial compressive tests were performed. Figure 27 depicts the test setup. A TAB connected to the machine is used to provide the first external configuration of the sample and preloading. During testing, the variance of the applied load and deformation behaviours for each sample are logged in a computer attached to the INSTRON machine. At a crosshead movement rate of 0.02 mm/sec and a normal atmospheric environment (27°C and 65 % RH), the samples are crushed. Finally, the data collected from the load and elongations of the tested samples are used to plot the average

stress–strain curves. The slope of the stress–strain curve is also used to calculate compressive elastic modulus. Figure 28 depicts the average stress–strain statistics based on the tree samples.

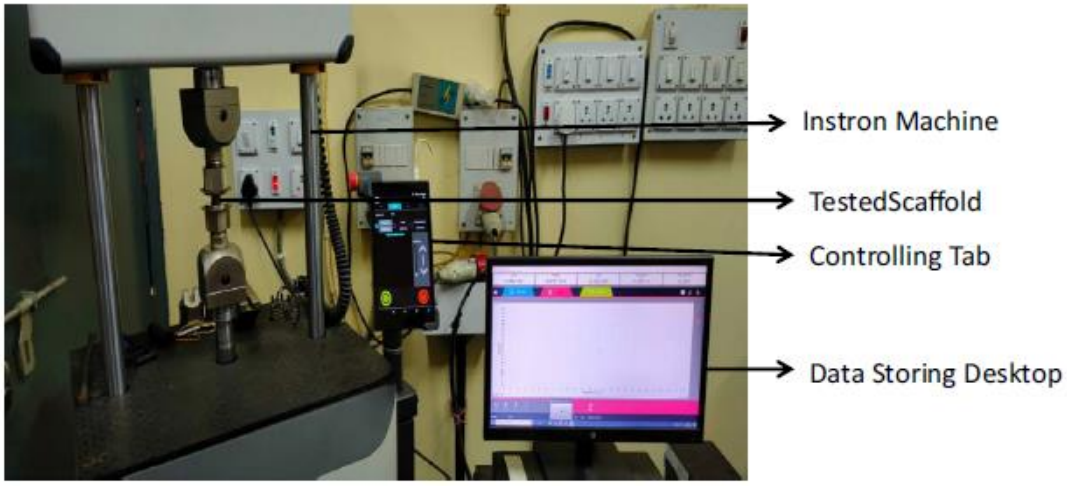

Figure 27: Experimental setup for compression test on INSTRON.

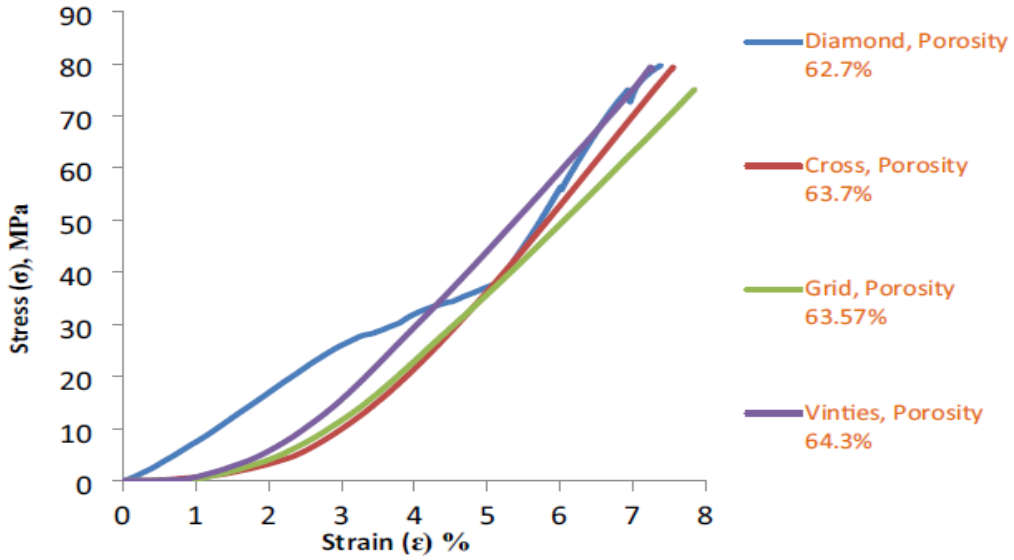

Figure 28: Stress–strain curve for compression test of scaffolds.

The slope of the graph is used to calculate the elastic modulus of the tested materials. The diamond, cross, grid, and vinties scaffolds have elastic moduli of 10.08, 11.15, 10.33, and 11.76 GPa, correspondingly. The compressive strength of diamond, cross, grid, and vinties scaffolds, on the other hand, is 79.685, 78.735, 75.1, and 79.328MPa, respectively. The test findings show that the diamond sample is slightly hard during first load application due to its shape, but as the single wire deforms, it abruptly softens and strain deformation accelerates. The elastic modulus of the fabricated scaffold seems promising, matching that of genuine cortical bones.Therefore, it

has a greater compressive strength than bone. (Bone has a compressive strength of 0.45–15.6 MPa [94].) This increased compressive strength reduces the stress shielding effect and extends the implant's lifetime.

The computer-modeled scaffold has a theoretical porosity of 65%. Therefore, maintaining the correct porosity during fabrication is challenging, and the scaffold porosity might deviate from the planned porosity. A correlation analysis was also carried out in order to utilise the modest deviated porosity. The elastic modulus and strength of porous materials are affected by porosity or relative density, and it is necessary to understand how elastic property varies with prepared samples. As a result, the Gibson–Ashby correlation model [95] is used in this work to investigate the relationship between porosity and elastic characteristics. The link between elastic modulus and strength and porosity is shown below:

$$E_1 / E_2 = C_1 (W_1 / W_2)^a \quad (7)$$

$$\sigma_1 / \sigma_2 = C_2 (W_1 / W_2)^b \quad (8)$$

Where E_1, W_1, and $\sigma_1$represent the elastic modulus, weight, and strength of porous scaffolds and E_2, W_2, and$\sigma_2$represent the elastic modulus, weight, and strength of Ti alloy, and a, b, C_1, and C_2 are the constants. Consider E_2 is equal to 110 GPa [96] and σ_2 is equal to 1096 MPa [97]. Using Eq. (6), Eqs. (7) and (8) can be rewritten as:

$$E_1 / E_2 = C_1 (1 - P)^a \quad (9)$$

$$\sigma_1 / \sigma_2 = C_2 (1 - P)^b \quad (10)$$

Where a = 2, b = 1.5, C_1= 1, and C_2 = 0.3 which are used as per Gibson–Ashby model [96].

Figure 29 depicts the relative elastic modulus (modulus ratio of porous scaffold to solid section) of the current samples with varying porosities. The relative elastic modulus decreases as the proportion of porosity increases. Relative compressive strength, on the other hand, is demonstrated in Figure 30 with varied porosity percentages, and relative compressive strength is shown to decrease with increasing porosity %. This relative elastic modulus and relative compressive strength can provide a suitable reference for the user-specific need, based on the implant bone's required strength for the desired application.

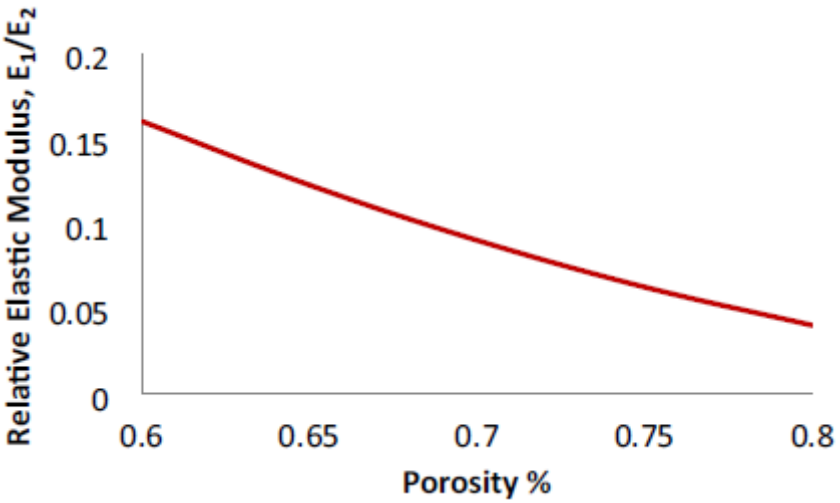

Figure 29: Relative elastic modulus, E_1/E_2vs porosity %.

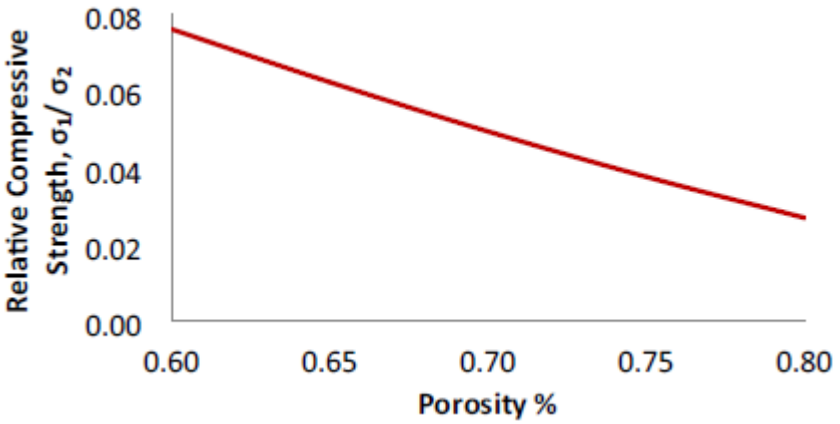

Figure 30: Relative compressive strength, σ_1/σ_2vs porosity %.

Chapter 5

Optimization of Porosity Results

The Taguchi analysis approach was used in the Design of Experiments (DOE). The porosity of the various samples was determined, and the findings were then evaluated for optimization using the Taguchi technique and the Minitab software. An optimization analysis of the percentage of porosity vs scan speed (mm/sec), hatch distance (mm), and laser power (W) is carried out. Mean and Signal to Noise ratio responses and graphs were produced. Every sample is studied at two levels, and the results are documented.

Minitab generates a table of estimated regression coefficients for each response feature. The signal-to-noise ratio (S/N) and the means are chosen as response characteristics in this investigation. The absolute value of the coefficient represents the relative importance of each element. The component with the highest coefficient has the most influence on a certain response characteristic. The amount of the factor coefficient in Taguchi designs generally corresponds to the factor rankings in the response tables.

The response tables display the average of each response characteristic for each factor level. The ranks in the tables are based on Delta statistics, which measure the relative size of impacts. The Delta statistic is calculated by taking the highest minus the lowest average for each element. Minitab assigns ranks based on Delta values, with rank 1 being the highest, rank 2 being the second highest, and so on. We always strive to optimise the S/N ratio in Taguchi trials.

The main effects graphs demonstrate how each component influences the response characteristic (S/N ratio, means). A major impact arises when various amounts of a component have varied effects on the characteristic. For a factor with two levels, we can see that one level raises the mean more than the other. This distinction is a significant consequence.

The main effects plot is generated by Minitab by plotting the typical average for each factor level. These averages correspond to those shown in the answer table.

a) There is no main impact when the line is horizontal. Each factor level has the same effect on the characteristic, and the characteristic average is the same across all factor levels.
b) There is a main effect when the line is not horizontal. Varied levels of the component have different effects on the feature. The size of the major effect increases with the difference in vertical position of the plotted points (the more the line is not parallel to the X-axis).

(A) Diamond

The main effects plots display the effect of different parameters and its extent in relation with porosity. In the scaffold of diamond, scan speed (mm/sec) shows huge variation in comparison to hatch distance (mm) and laser power (W). The porosity is greatly affected by the scan speed and thereby it is ranked 1 in the response tables for signal to ratio and means. The slope of scan speed is more inclined towards the vertical axis i.e. showing major deviation from horizontal axis therefore establishing higher impact upon porosity. Table 11 and 12 shows the response table for signal to noise ratio and figure 31 represents the main effect plots for signal to noise ratio and means. In the diamond scaffold, laser power is ranked second, and lastly the hatch distance. These parameters are ranked on the basis of their effect on the porosity of the scaffold.

Table 11: Response Table for Signal to Noise Ratio.

Level	**Scan speed (mm/sec)**	**Hatch Distance (mm)**	**Laser Power (W)**
1	35.92	36.1	36.14
2	36.29	36.11	36.08
Delta	0.37	0.01	0.05
Rank	1	3	2

Table 12: Response Table for Means.

Level	Scan speed (mm/sec)	Hatch Distance (mm)	Laser Power (W)
1	62.55	63.85	64.1
2	65.25	63.95	63.7
Delta	2.7	0.1	0.4
Rank	1	3	2

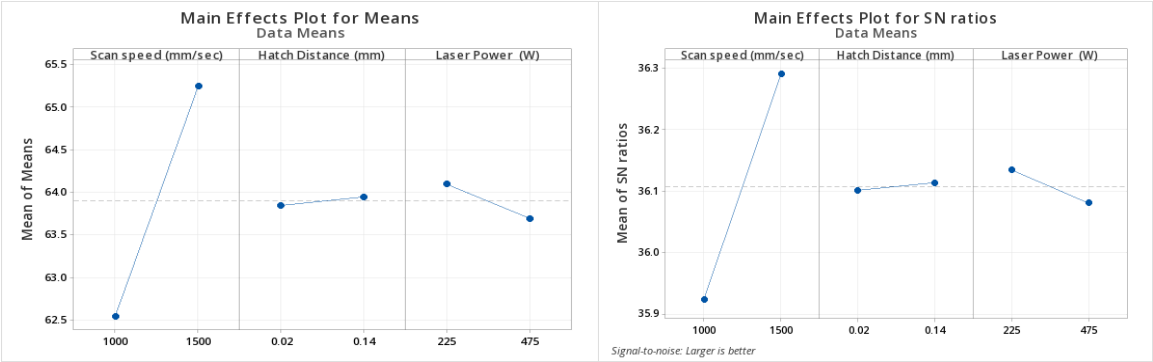

Figure 31: Main Effects Plots for Means and SN Ratios for Diamond.

(B) Cross

The main effects plots display the effect of different parameters and its extent in relation with porosity. In the cross scaffold, scan speed (mm/sec) shows huge variation in comparison to hatch distance (mm) and laser power (W). The porosity is greatly affected by the scan speed and thereby it is ranked 1 in the response tables for signal to ratio and means. The slope of scan speed is more inclined towards the vertical axis i.e. showing major deviation from horizontal axis, therefore, establishing a higher impact upon porosity. Table 13 and 14 shows the response table for signal-to-noise ratio and figure 32 represents the main effect plots for signal-to-noise ratio and means. In this scaffold, hatch distance is ranked second, and lastly the laser power.

Table 13: Response Table for Signal to Noise Ratios

Level	Scan speed (mm/sec)	Hatch Distance (mm)	Laser Power (W)
1	36.07	36.15	36.18
2	36.29	36.21	36.18
Delta	0.22	0.06	0.01
Rank	1	2	3

Table 14: Response Table for Means.

Level	Scan speed (mm/sec)	Hatch Distance (mm)	Laser Power (W)
1	63.6	64.2	64.45
2	65.25	64.65	64.4
Delta	1.65	0.45	0.05
Rank	1	2	3

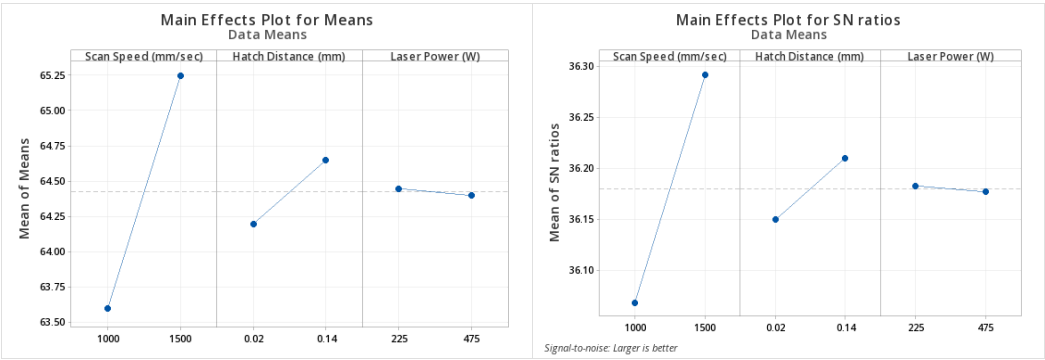

Figure 32: Main Effects Plots for Means and SN Ratios for Cross.

(C) Grid

The main effects plots display the effect of different parameters and its extent in relation with porosity. In the grid scaffold, scan speed (mm/sec) shows huge variation in comparison to hatch distance (mm) and laser power (W). The porosity is greatly affected by the scan speed and thereby it is ranked 1 in the response tables for signal to ratio and means. The slope of scan speed is more inclined towards the vertical axis i.e. showing major deviation from horizontal axis therefore establishing higher impact upon porosity. Table 15 and 16 shows the response table for

signal to noise ratio and figure 33 represents the main effect plots for signal-to-noise ratio and means. In this grid scaffold, hatch distance is ranked second and lastly the laser power. Hatch distance also shows greater impact on porosity as compared to the Diamond and Cross structures. Although laser power is comparatively similar to previous scaffolds.

Table 15: Response Table for Signal to Noise Ratios.

Level	Scan speed (mm/sec)	Hatch Distance (mm)	Laser Power (W)
1	36.17	36.2	36.24
2	36.29	36.26	36.22
Delta	0.12	0.05	0.01
Rank	1	2	3

Table 16: Response Table for Means.

Level	Scan speed (mm/sec)	Hatch Distance (mm)	Laser Power (W)
1	64.35	64.6	64.85
2	65.25	65	64.75
Delta	0.9	0.4	0.1
Rank	1	2	3

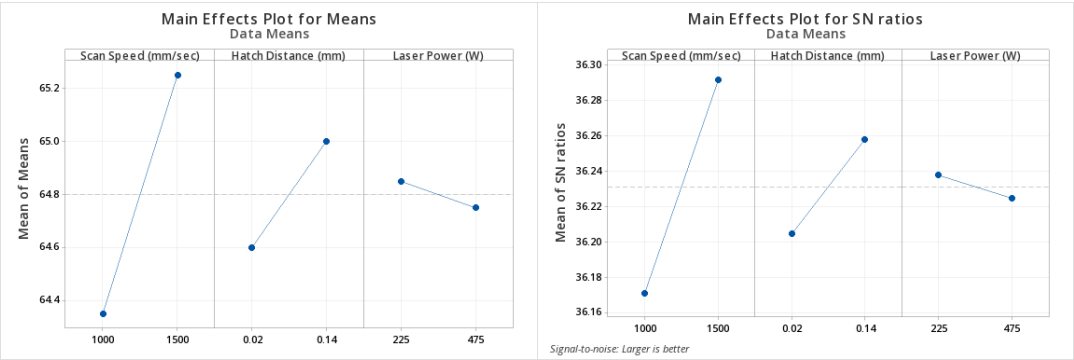

Figure 33: Main Effects Plots for Means and SN Ratios for Grid.

(D) Vinties

The main effects plots display the effect of different parameters and its extent in relation with porosity. In the vinties scaffold, scan speed (mm/sec) shows huge variation in comparison to hatch distance (mm) and laser power (W). The porosity is greatly affected by the scan speed and thereby it is ranked 1 in the response tables for signal to ratio and means. The slope of scan speed is more inclined towards the vertical axis i.e. showing major deviation from horizontal axis therefore establishing higher impact upon porosity. Table 17 and 18 shows the response table for signal to noise ratio and figure 34 represents the main effect plots for signal to noise ratio and means. In this vinties scaffold, hatch distance is ranked second and lastly the laser power. Hatch distance also shows greater impact on porosity as compared to the Diamond and Cross structures. In this case laser power is also having significantly much impact in comparison to Diamond, Cross and Vinties scaffold.

Table 17: Response Table for Signal to Noise Ratio.

Level	**Scan speed (mm/sec)**	**Hatch Distance (mm)**	**Laser Power (W)**
1	36.19	36.22	36.25
2	36.29	36.26	36.23
Delta	0.1	0.05	0.02
Rank	1	2	3

Table 18: Response Table for Means.

Level	**Scan speed (mm/sec)**	**Hatch Distance (mm)**	**Laser Power (W)**
1	64.5	64.7	64.95
2	65.25	65.05	64.8
Delta	0.75	0.35	0.15
Rank	1	2	3

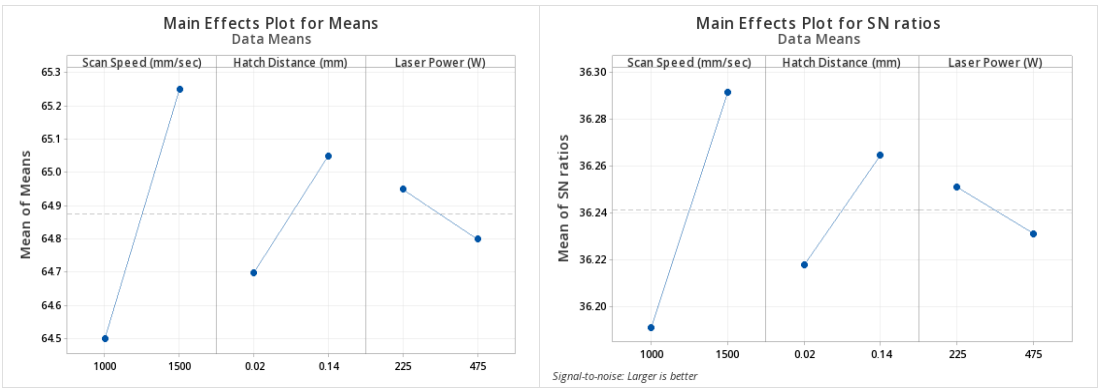

Figure 34: Main Effects Plots for Means and SN Ratios for Vinties.

Chapter 6

Microscopic Study of Scaffolds

The scaffolds are modeled, fabricated employing the method of Selective Laser Melting (SLM) and different mechanical tests were performed on each scaffold. Further, optimization of the porosity results with other parameters such as scanning speed (mm/sec), hatch distance (mm) and laser power were carried out using Taguchi methodology in Minitab. This chapter deals with the microscopic study that was performed on each scaffold which enables to determine the pore size and the strut thickness of each scaffold and also certain angles which were possible to compute for certain geometry.

An Optical microscope/Stereo microscope (ZEISS Stemi 508) was employed for the microscopic examination of the scaffolds. The Stereo microscope employed in this work is shown in the figure 35. The characteristics of this microscope are presented in the table 19.

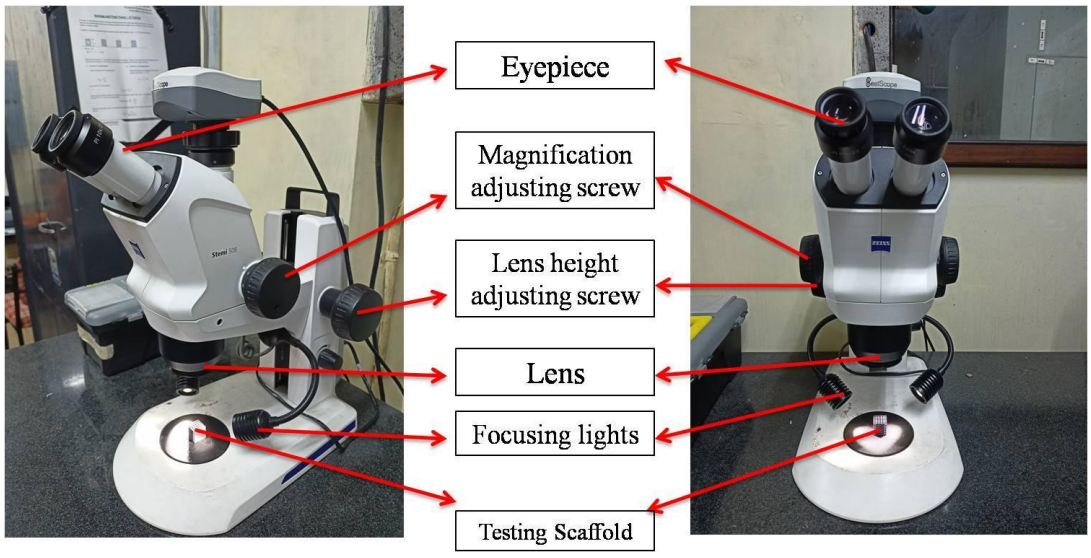

Figure 35: The Stereo Microscope (ZEISS Stemi 508).

Table 19: General specifications of the microscope.

Type of Microscope	Stereo microscope, Greenough design
Design Principle	Two zoom systems, tilted by the stereo angle
Stereoscopic View	Three dimensional observation through eyepieces
Apochromatic Corrected Zoom and Front Optics	Image free of color fringes in complete magnification range
Manual Zoom, Zoom Range	8:1 (0.63×...5.0×)
Quality of Zoom Optics	Distortion free, excellent contrast, apochromatic corrected
Ergonomic Viewing Angle	35°
Adjustment of Interocular Distance	55 – 75 mm
Eyepieces	d = 30 mm
Stemi Mounts	d = 76 mm
Illuminators	d = 53 mm; Illuminators d = 66 mm via clamp ring d53/66
Working Surface	W255 × D215 mm
Height / Lifting range	360 mm / 190 mm
Load capacity of Stemi mount	5 kg

(A) Diamond

Each scaffold was examined under the microscope for the determination of its pore size and strut thickness. The pore size is determined by the maximum possible polygon that could be fitted in the microscopic image of the scaffold which further records the possibe area of the pore size.

For the case of diamond the pore size was observed to be between 496405.053µm^2 to 586787.302µm^2. The strut thickness was found to be in the range of 480.724µm to 513.315µm. In the diamond scaffold the angles of the pore geometry was also observed and were found to be between 93.7° to 105.9°. Figure 36 show the microscopic image of the diamond scaffold and figure 37 shows the diamond scaffold presenting all the observed markings in the scaffold.

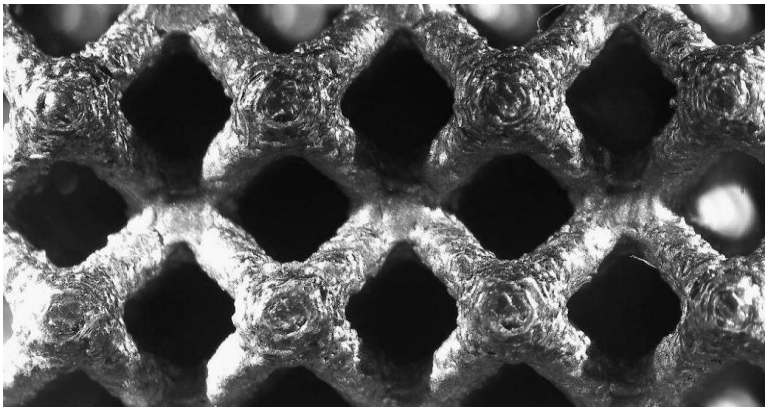

Figure 36: Microscopic image of diamond scaffold.

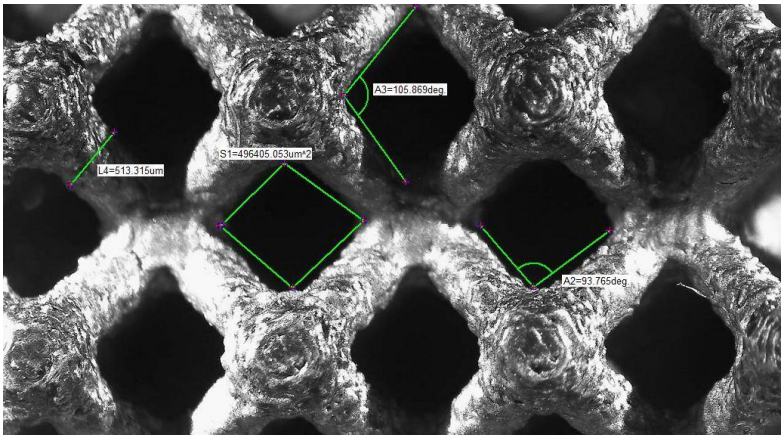

Figure 37: Microscopic image of diamond scaffold with observed markings.

(B) Cross

In the case of cross scaffold the pore size was observed to be around 1250734.222µm^2. The strut thickness was found to be in the range of 708.282µm to 714.086µm. Figure 38 show the microscopic image of the cross scaffold and figure 39 shows the cross scaffold presenting all the observed markings in the scaffold.

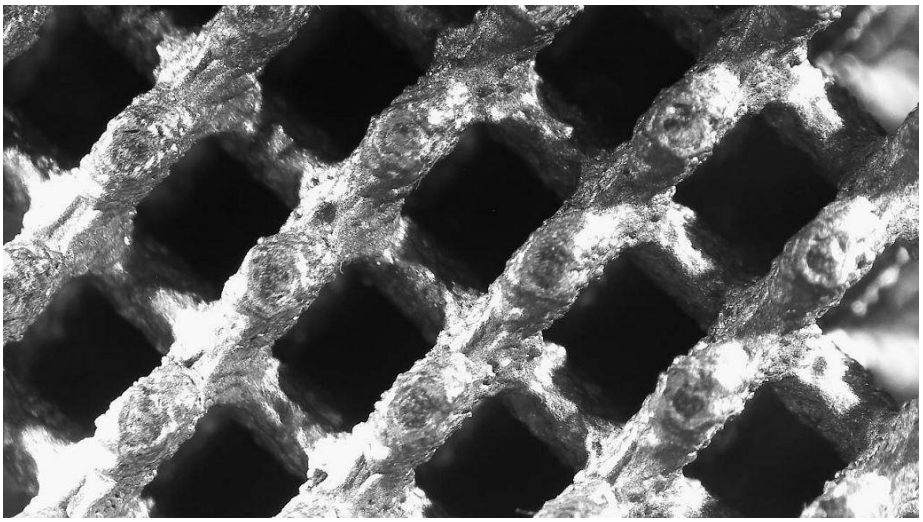

Figure 38: Microscopic image of cross scaffold.

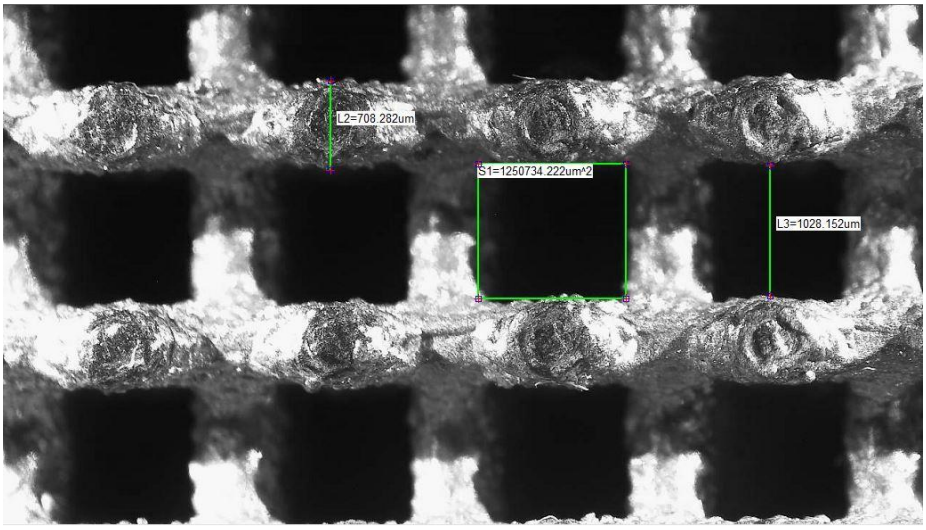

Figure 39: Microscopic image of cross scaffold with observed markings.

(C) Grid

In the grid scaffold the pore size was observed to be in the range of 1477810.199µm^2 to 2417618.517 µm^2. The strut thickness was found to be in the range of 668.244µm to 1011.161µm. Figure 40 shows the microscopic image of the grid scaffold and figure 41 shows the grid scaffold presenting all the observed markings in the scaffold.

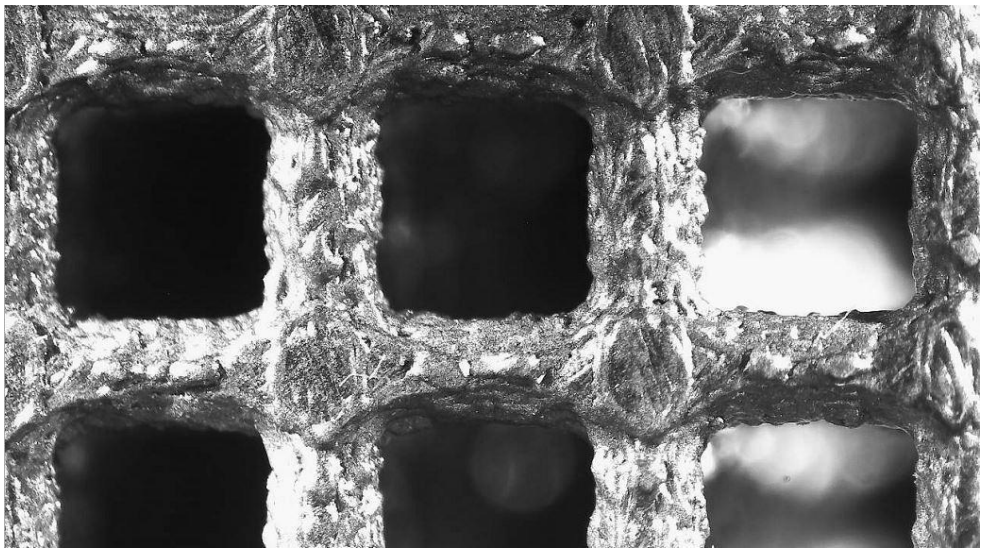

Figure 40: Microscopic image of grid scaffold.

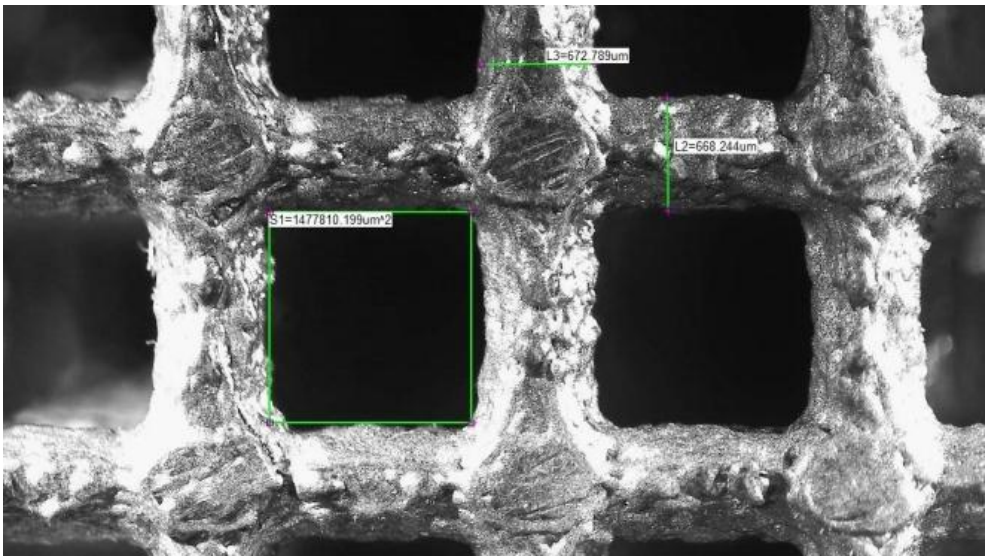

Figure 41: Microscopic image of grid scaffold with observed markings.

(D) Vinties

In the vinties scaffold the pore size was observed in the form of a circular area unlike other scaffolds and found to be in the range of 1272214.375µm^2 to 1290453.750µm^2. The strut thickness was found to be in the range of 327.304µm to 427.297µm. Figure 42 shows the microscopic image of the vinties scaffold and figure 43 shows the vinties scaffold presenting all the observed markings in the scaffold.

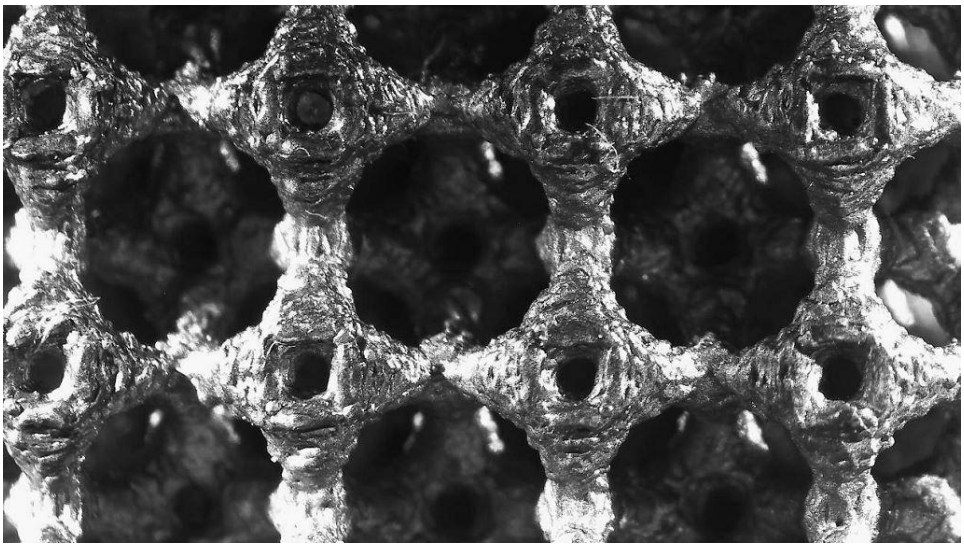

Figure 42: Microscopic image of vinties scaffold.

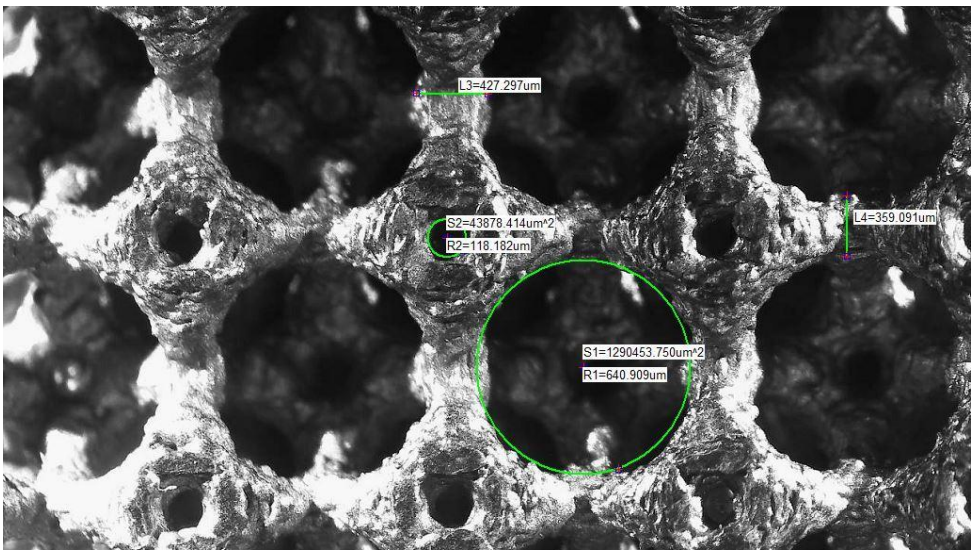

Figure 43: Microscopic image of vinties scaffold with observed markings.

Chapter 7

Conclusions

The selective laser melting (SLM) technology is used to create porous Ti-6Al-4V scaffolds for biological purposes. For the acceptability of a biomedical implant, porosity, surface roughness, and mechanical compression tests are done. To employ the porosity deviated scaffold, the relative elastic modulus is also investigated. Optimization and microscopic studies of the fabricated scaffolds were also performed. The following findings may be drawn from the current work.

a) Because the metal powder is adhered to the wire surface, the strut diameters of 3D-printed scaffold are somewhat larger than the specified diameter during printing. As a result, the porosities of AM-fabricated scaffolds are somewhat smaller than those of planned scaffolds, resulting in relative differences in elastic modulus and mechanical strength. The grid-type sample has the lowest error percentage, while the diamond type has the greatest porosity difference, and the grid-type sample may provide better likeness with the lowest deviation.
b) The grid scaffolds do not require surface treatment because they have a R_a value of 24.9 µm. The other three varieties, on the other hand, require surface treatment. The grid-type structure's strut diameter is simpler and easier to build, resulting in a better surface polish. The grid-type sample has the lowest surface roughness value, but the diamond-type sample has a greater surface roughness value.
c) The elastic modulus of the produced porous scaffold (with 65 % porosity) is excellently matched to that of human bone, but the compressive strength is superior to that of human bone, which will assist to lessen the stress shielding effect and extend the implant's lifetime.

d) The relative elastic modulus & relative compressive strength can provide a convenient reference for the user-specific need based on the implant bone's required strength for the desired application. It will aid in tailoring the porosity percentage for patient- and bone-specific implants.
e) The microstructure of porous Ti64 alloy scaffolds could be regulated by SLM by adjusting the processing parameters that are: 340W laser power, 1250mm/s scanning speed, 0.12 mm powder layer thickness, and 0.06 mm hatch spacing.
f) The maximum ultimate compressive strength for grid type scaffolds with a height strut thickness of 740.249m was discovered to be 101.39 MPa, which is equal to human bone.
g) Titanium alloys have been successfully connected in biomedical sectors as a result of additive technologies, which have the ability to create any sophisticated porous scaffold for biomedical applications, and therefore provide further assistance for material engineers and prospective designers.

Future Scope of Work

The following future research directions are recommended:

Recent statistical modeling of lattice structure manufacturing utilizing SLM has revealed the essential processing factors influencing lattice structure attributes. To validate the effects, the work might be expanded to include thermal modeling of thin struts or the entire three-dimensional (3D) lattice systems. The experimental data acquired in this study may then be used to validate the thermal models.

Apatite forming ability, live/dead viability cytotoxicity, and alkaline phosphatase activity can be used to gain further biological responses. The dynamic habitat could also be employed since the behaviour of planted cells on scaffolds differs in static and dynamic environments.

Histological tests may be performed to determine the path travelled by cells in vitro to penetrate the scaffolds.

More testing with regard to the physical and biocompatible qualities is necessary to have a better understanding of the possibilities for this innovative method in producing porous Ti scaffolds for hard tissue engineering.

Enhance the accuracy of findings by adhering to orthopaedic implant testing standards to guarantee accurate and consistent testing. Examine the scaffolds' additional mechanical qualities and their potential for hard tissue engineering.

References

[1] Nouri A, Hodgson PD, Wen C. Biomimetic porous titanium scaffolds for orthopedic and dental applications. 2010.

[2] Banhart J. Manufacture, characterisation and application of cellular metals and metal foams. Progress in materials Science 2001;46(6):559-632.

[3] Barbucci R. Integrated biomaterials science. : Springer; 2002.

[4] Brailovski V, Prokoshkin S, Gauthier M, Inaekyan K, Dubinskiy S. Mechanical properties of porous metastable beta Ti–Nb–Zr alloys for biomedical applications. J Alloys Compounds 2013;577:S413-S417.

[5] Bram M, Stiller C, Buchkremer HP, Stöver D, Baur H. High-Porosity Titanium, Stainless Steel, and Superalloy Parts. Advanced Engineering Materials 2000;2(4):196- 199.

[6] Breme J, Eisenbarth E, Biehl V. Titanium and its alloys for medical applications. Titanium and Titanium Alloys: Fundamentals and Applications 2003:423-451.

[7] Dezfuli SN, Sadrnezhaad S, Shokrgozar M, Bonakdar S. Fabrication of biocompatible titanium scaffolds using space holder technique. J Mater Sci Mater Med 2012;23(10):2483-2488.

[8] Oh I, Nomura N, Masahashi N, Hanada S. Mechanical properties of porous titanium compacts prepared by powder sintering. Scr Mater 2003;49(12):1197-1202.

[9] E. Marin, M. Pressacco, S. Fusi, A. Lanzutti, S. Turchet, L. Fedrizzi, Characterization of grade 2 commercially pure Trabecular Titanium structures. Mater. Sci. Eng.: C 33, 2648–2656 (2013).

[10] D.K. Pattanayak, A. Fukuda, T. Matsushita, M. Takemoto, S. Fujibayashi, K. Sasaki, N. Nishida, T. Nakamura, T. Kokubo, Bioactive Ti metal analogous to human cancellous bone: Fabrication by selective laser melting and chemical treatments. Acta Biomaterialia 7, 1398–1406 (2011).

[11] F. Abe, E.C. Santos, Y. Kitamura, K. Osakada, M. Shiomi, Influence of forming conditions on the titanium model in rapid prototyping with the selective laser melting process. Proc. Inst. Mech. Eng. Part C—J. Mech. Eng. Sci. 217, 119–126 (2003).

[12] Imam, M.A., Froes, F. “Low cost Titanium and developing applications”. The Journal of The Minerals, Metals and Materials Society (TMS), 2010, 62.5: 17-20.

[13] Lütjering, G., Williams, JC. “Titanium”. Springer-Verlag, 2007.

[14] Gibson, I, Rosen, D.W., Stucker, B. “Additive Manufacturing Technologies: Rapid Prototyping to Direct Digital Manufacturing”. Springer, 2010.

[15] ASTM international. ASTM standard F2792-12a: Terminology for Additive Manufacturing Technologies. DOI 10.1520/F2792-12A, 2012.

[16] Wohlers, T and Caffrey, T. Wohlers report 2013. Tech. rep., Wohlers associates, 2013. ISBN 0-9754429-9-6.

[17] Koike, M., Greer, P., Owen, K., Lilly, G., Murr, L. E., Gaytan, S. M., Martinez, E., and Okabe, T. Evaluation of titanium alloys fabricated using rapid prototyping technologies - electron beam melting and laser beam melting. Materials 4, 10 (2011), 1776–1792.

[18] Murr, L., Quinones, S., Gaytan, S., Lopez, M., Rodela, A., Martinez, E., Hernandez, D., Martinez, E., Medina, F., and Wicker, R. Microstructure and mechanical behavior of Ti–6Al–4V produced by rapid-layer manufacturing, for biomedical applications. Journal of the Mechanical Behavior of Biomedical Materials 2, 1 (2009), 20–32.

[19] Brice, C., Rosenberger, B., Sankaran, S., Taminger, K., Woods, B., and Nasserrafi, R. Chemistry control in electron beam deposited titanium alloys. Materials Science Forum 618-619 (2009), 155–158.

[20] Kruth, J.-P., Levy, G., Klocke, F., and Childs, T. Consolidation phenomena in laser and powder-bed based layered manufacturing. CIRP Annals-Manufacturing Technology 56, 2 (2007), 730–759.

[21] Lütjering, G., & Williams, J. C. (2003). Ti / Gerd Lütjering, James Williams. New York: New York : Springer.

[22] Lütjering, G. W., J. C., Gysler. A. Microstructure and Mechanical Properties of Ti Alloys. Retrieved from http://wwweng.lbl.gov/~shuman/NEXT/MATERIALS&COMPONENTS/Pressure_vessels/Ti_4311_chap01.pdf

[23] Polmear, I. (2005). Light Alloys From Traditional Alloys to Nanocrystals (4th ed.. ed.). Burlington: Burlington : Elsevier Science.

[24] Meng-Qi, C., Tuerhongjiang, W., Guo-Feng, J., Wei, L., Yu-Qin, Q., Xiao-Chun, P., . . . Xuan-Yong, L. (2016). A novel open-porous magnesium scaffold with controllable microstructures and properties for bone regeneration. Scientific Reports, 6. doi:10.1038/srep24134

[25] Long, M., & Rack, H. J. (1998). Ti alloys in total joint replacement—a materials science perspective. Biomaterials, 19(18), 1621-1639. doi:10.1016/S0142-9612(97)00146-4

[26] Lü tjering, G., & Williams, J. C. (2007). Ti (2nd ed.. ed.). Berlin, Heidelberg: Berlin, Heidelberg : Springer Berlin Heidelberg.

[27] Li, Y., Yang, C., Zhao, H. D., Qu, S. G., Li, X., & Li, Y. (2014). New Developments of Ti-Based Alloys for Biomedical Applications. In Materials (Vol. 7, pp. 1709-1800).

[28] Choi, K., Kuhn, J. L., Ciarelli, M. J., & Goldstein, S. A. (1990). The elastic moduli of human subchondral, trabecular, and cortical bone tissue and the size-dependency of cortical bone modulus. Journal of Biomechanics, 23(11), 1103-1113. doi:10.1016/0021-9290(90)90003-L

[29] Wang, X., Chen, X., Hodgson, P. D., & Wen, C. E. (2006). Elastic modulus and hardness of cortical and trabecular bovine bone measured by nanoindentation. Transactions of Nonferrous Metals Society of China, 16, s744-s748. doi:10.1016/S1003- 6326(06)60293-8

[30] Elias, C., Lima, J., Valiev, R., & Meyers, M. (2008). Biomedical applications of Ti and its alloys. The Journal of The Minerals, Metals & Materials Society (TMS), 60(3), 46-49. doi:10.1007/s11837-008-0031-1

[31] Parthasarathy, J., Starly, B., Raman, S., & Christensen, A. (2010). Mechanical evaluation of porous Ti (Ti6Al4V) structures with electron beam melting (EBM). Journal of the Mechanical Behavior of Biomedical Materials, 3(3), 249-259. doi:10.1016/j.jmbbm.2009.10.006

[32] Ryan, G., Pandit, A., & Apatsidis, D. P. (2006). Fabrication methods of porous metals for use in orthopaedic applications. Biomaterials, 27(13), 2651-2670. doi:10.1016/j.biomaterials.2005.12.002

[33] M. Niinomi, Biomaterials 2003, 24, 2673.

[34] S. E. Haghighi, H. B. Lu, G. Y. Jian, G. H. Cao,D. Habibi, L. C. Zhang, Mater. Des. 2015, 76, 47.

[35] M. Niinomi, M. Nakai, J. Hieda, Acta Biomater. 2012,8, 3888.

[36] S. J. Li, T. C. Cui, Y. L. Hao, R. Yang, Acta Biomater.2008, 4, 305.

[37] Y. H. Li, C. Yang, H. D. Zhao, S. G. Qu, X. Q. Li,Y. Y. Li, Materials 2014, 7, 1709.

[38] Y. L. Hao, S. J. Li, S. Y. Sun, C. Y. Zheng, Q. M. Hu, R. Yang, Appl. Phys. Lett. 2005, 87, 1906.

[39] X. Y. Cheng, S. J. Li, L. E. Murr, Z. B. Zhang, Y. L. Hao, R. Yang, F. Medina, R. B.Wicker, J. Mech. Behav. Biomed. Mater. 2012, 16, 153.

[40] H. Attar, M. B€onisch, M. Calin, L. C. Zhang, K. Zhuravleva, A. Funk, S. Scudino, C. Yang, J. Eckert, J. Mater. Res. 2014, 29, 1941.

[41] H. Attar, L. L€ober, A. Funk, M. Calin, L. C. Zhang, K. G. Prashanth, S. Scudino, Y. S. Zhang, J. Eckert, Mater. Sci. Eng. A 2015, 625, 350.

[42] V. J. Challis, A. P. Roberts, J. F. Grotowski, L. C. Zhang, T. B. Sercombe, Adv. Eng. Mater. 2010, 12, 1106.

[43] V. J. Challis, X. X. Xu, L. C. Zhang, A. P. Roberts, J. F. Grotowski, T. B. Sercombe, Mater. Des. 2014, 63, 783.

[44] A. Barbas, A. S. Bonnet, P. Lipinski, R. Pesci, G. Dubois, J. Mech. Behav. Biomed. Mater. 2012, 9, 34.

[45] M. Geetha, A. K. Singh, R. Asokamani, A. K. Gogia, Prog. Mater. Sci. 2009, 54, 397.

[46] L. C. Zhang, H. Attar,M. Calin, J. Eckert, Mater. Technol. 2016, 31, 66.

[47] L. C. Zhang, H. Attar, Adv. Eng. Mater. 2016, 18, 463.

[48] H. Attar, M. Bönisch, M. Calin, L. C. Zhang, S. Scudino, J. Eckert, Acta Mater. 2014, 76, 13.

[49] Y. J. Liu, S. J. Li, L. C. Zhang, Y. L. Hao, T. B. Sercombe, Scr. Mater. 2018, 153, 99.

[50] H. Attar, M. Bönisch, M. Calin, L. C. Zhang, K. Zhuravleva, A. Funk, S. Scudino, C. Yang, J. Eckert, J. Mater. Res. 2014, 29, 1941.

[51] L. Thijs, F. Verhaeghe, T. Craeghs, J. Van Humbeeck, J.-P. Kruth, Acta Mater. 2010, 58, 3303.

[52] Y. Yang, Y. Chen, J. Zhang, X. Gu, P. Qin, N. Dai, X. Li, J.-P. Kruth, L.-C. Zhang, Mater. Des. 2018, 146, 239.

[53] H. Attar, K. G. Prashanth, A. K. Chaubey, M. Calin, L. C. Zhang, S. Scudino, J. Eckert, Mater. Lett. 2015, 142, 38.

[54] M. F. Lopez, A. Gutierrez, J. A. Jimenez, Electrochim. Acta 2002, 47, 1359.

[55] E. Chlebus, B. Kuznicka, T. Kurzynowski, B. Dybała, Mater. Charact. 2011, 62, 488.

[56] Y. J. Liu, X. P. Li, L. C. Zhang, T. B. Sercombe, Mater. Sci. Eng. A 2015, 642, 268.

[57] L. C. Zhang, T. B. Sercombe, Key Eng. Mater. 2012, 520, 226.

[58] N. Dai, L. C. Zhang, J. Zhang, Q. Chen, M. Wu, Corros. Sci. 2016, 102, 484.

[59] N. Dai, J. Zhang, Y. Chen, L. C. Zhang, J. Electrochem. Soc. 2017, 164, C428.

[60] Y. Chen, J. Zhang, N. Dai, P. Qin, H. Attar, L. C. Zhang, Electrochim. Acta 2017, 232, 89

[61] L.-C. Zhang, Y. Liu, S. Li, Y. Hao, Adv. Eng. Mater. 2018, 20, 1700842.

[62] Y. J. Liu, S. J. Li, H. L. Wang, W. T. Hou, Y. L. Hao, R. Yang, T. B. Sercombe, L. C. Zhang, Acta Mater. 2016, 113, 56.

[63] X. Gong, Y. Li, Y. Nie, Z. Huang, F. Liu, L. Huang, L. Jiang, H. Mei, Corros. Sci. 2018

[64] Y. Bai, X. Gai, S. Li, L.-C. Zhang, Y. Liu, Y. Hao, X. Zhang, R. Yang, Y. Gao, Corros. Sci. 2017, 123, 289.

[65] C. De Formanoir, S. Michotte, O. Rigo, L. Germain, S. Godet, Mater. Sci. Eng. A 2016, 652, 105.

[66] L. Thijs, F. Verhaeghe, T. Craeghs, J. Van Humbeeck, J.-P. Kruth, Acta Mater. 2010, 58, 3303.

[67] X. Wang, Y. Li, J. Xiong, P. D. Hodgson, C. Wen, Acta Biomater. 2009, 5, 3616.

[68] C. E. Wen, M. Mabuchi, Y. Yamada, K. Shimojima, Y. Chino, T. Asahina, Scr. Mater. 2001, 45, 1147.

[69] X. Zhao, H. Sun, L. Lan, J. Huang, H. Zhang, Y. Wang, Mater. Lett. 2009, 63, 2402.

[70] Y. J. Liu, H. L. Wang, S. J. Li, S. G. Wang, W. J. Wang, W. T. Hou, Y. L. Hao, R. Yang, L. C. Zhang, Acta Mater. 2017, 126, 58.

[71] K. Asaoka, N. Kuwayama, O. Okuno, I. Miura, J. Biomed. Mater. Res. 1985, 19, 699.

[72] C. Yang, L. M. Kang, X. X. Li, W. W. Zhang, D. T. Zhang, Z. Q. Fu, Y. Y. Li, L. C. Zhang, E. J. Lavernia, Acta Mater. 2017, 132, 491.

[73] Z. A. Munir, U. Anselmi-Tamburini, M. Ohyanagi, J. Mater. Sci. 2006, 41, 763.

[74] R. Nicula, F. Lüthen, M. Stir, B. Nebe, E. Burkel, Biomol. Eng. 2007, 24, 564.

[75] F. Zhang, E. Otterstein, E. Burkel, Adv. Eng. Mater. 2010, 12, 863.

[76] A. Ibrahim, F. Zhang, E. Otterstein, E. Burkel, Mater. Des. 2011, 32, 146.

[77] Y. Y. Li, L. M. Zou, C. Yang, Y. H. Li, L. J. Li, Mater. Sci. Eng. A 2013, 560, 857.

[78] J. P. Kruth, P. Mercelis, J. Van Vaerenbergh, L. Froyen, M. Rombouts, Rapid Prototyp. J. 2005, 11, 26.

[79] L. C. Zhang, D. Klemm, J. Eckert, Y. L. Hao, T. B. Sercombe, Scripta Mater. 2011, 65, 21.

[80] C. Y. Lin, T. Wirtz, F. LaMarca, S. J. Hollister, J. Biomed. Mater. Res. A 2007, 83, 272

[81] J. F. Isaza, P. C. Aumund-Kopp, Powder Metall. Rev. 2014, 3, 41.

[82] R. Morgan, C. J. Sutcliffe, W. O'Neill, Rapid Prototyp. J. 2001, 7, 159.

[83] H. Attar, M. Calin, L. C. Zhang, S. Scudino, J. Eckert, Mater. Sci. Eng. A 2014, 593, 170.

[84] T. Marcu, M. Todea, I. Gligor, P. Berce, C. Popa, Appl. Surf. Sci. 2012, 258, 3276.

[85] Zilberman, M. (2011). Active Implants and Scaffolds for Tissue Regeneration. Berlin, Heidelberg: Berlin, Heidelberg : Springer Berlin Heidelberg.

[86] Gibson, L. J. (1985). The mechanical behaviour of cancellous bone. Journal of Biomechanics, 18(5), 317-328. doi:10.1016/0021-9290(85)90287-8

[87] Hansma, P. (2004). AFM and SEM Imaging of Bone. Retrieved fromhttp://hansmalab.physics.ucsb.edu/afmbone.html

[88] B. Vandenbroucke, J.-P. Kruth, Selective laser melting of biocompatible metals for rapid manufacturing of medical parts, Rapid Prototyp. J. 13 (2007) 196-203.

[89] Y. Liu, Y. Yang, S. Mai, D. Wang, C. Song, Investigation into spatter behavior during selective laser melting of AISI 316L stainless steel powder, Mater. Des. 87 (2015) 797-806.

[90] H. Attar, M. Bermingham, S. Ehtemam-Haghighi, A. Dehghan-Manshadi, D. Kent, M. Dargusch, Evaluation of the Mechanical and Wear Properties of Titanium Produced by Three Different Additive Manufacturing Methods for Biomedical Application, Mater. Sci. & Eng.: A 760 (2019) 339-345.

[91] L. Le Guehennec, M.A. Lopez-Heredia, B. Enkel et al., Osteoblastic cell behaviour on different titanium implant surfaces. Actabiomaterialia. 4(3), 535–543 (2008).

[92] L. Le Gue´hennec, A. Soueidan, P. Layrolle et al., Surface treatments of titanium dental implants for rapid osseointegration. Dent. Mater. 23(7), 844–854 (2007).

[93] S. Ponader, E. Vairaktaris, P. Heinl et al., Effects of topographical surface modifications of electron beam melted Ti-6Al-4V titanium on human fetal osteoblasts. J. Biomed. Mater. Res., Part A 84(4), 1111–1119 (2008).

[94] M.V. Martens, R. Van Audekercke, P. Delport et al., The mechanical characteristics of cancellous bone at the upper femoral region. J. Biomech. 16(12), 971–983 (1983).

[95] M.F. Ashby, L.J. Gibson, Cellular solids structure and properties. Press Synd. Univ. Cambridge: Cambridge, UK. 175–231 (1997).

[96] T. Vilaro, C. Colin, J.D. Bartout, As-fabricated and heat-treated microstructures of the Ti-6Al-4V alloy processed by selective laser melting. Metall. Mater. Trans. A. 42(10), 3190–3199 (2011).

[97] S. Liu, Y.C. Shin, Additive manufacturing of Ti6Al4V alloy: A review. Mater. Design. 164, 107552 (2019).